# 16

# The Polar Cap PC Indices: Relations to Solar Wind and Global Disturbances

Peter Stauning
*Danish Meteorological Institute*
*Denmark*

## 1. Introduction

The solar wind plasma flow impinging on the Earths magnetosphere causes a range of geophysical disturbances such as magnetic storms and substorms, energization of the plasma trapped in the Earth's near space, auroral activity, and Joule heating of the upper atmosphere. Auroral activity was characterized already in 1961 by the electrojet indices (AU, AL, AE and AO) based on magnetic observations at auroral latitudes (Davis & Sugiura, 1966). On the contrary, several attempts have been made in the past to scale high-latitude disturbances on basis of polar magnetic variations without reaching a final, agreed and IAGA-adopted Polar Cap index. Fairfield (1968) suggested that the maximum amplitude of the magnetic variations observed from a ring of polar cap observatories could be a better indicator of the overall high-latitude magnetic activity than the auroral electrojet indices. He also noted that the Polar Cap "magnetic activity magnitude" sometimes increased before changes in the AE index.

Kuznetsov & Troshichev (1977) defined a "$PC_L$" index based on the variability of high-latitude magnetic recordings (much like the K indices), and not equivalent to the present PC "level index". Later, a "PC(Bz)" index based on a composite of the variance and the level of polar magnetic activity was proposed by Troshichev et al. (1979), who used the Polar Cap magnetic activity as a signature of substorm development. The "MAGPC" index suggested by Troshichev & Andrezen (1985) was based on the magnitude (in nT) of 15 min samples of the magnetic variation in the direction of the 03:00-15:00 MLT meridian. The MAGPC index was introduced to provide a measure of the solar wind electric field to be derived from available ground-based magnetic observations in the central Polar Cap. A major problem for these initial "PC" indices was their dependence on the daily and seasonal changes in the ionospheric conductivity with the varying solar illumination. Such variations cause corresponding variations in the "sensitivity" of the disturbance indices in their response to varying solar wind conditions.

The present version of a Polar Cap (PC) index is based on the formulation by Troshichev et al. (1988). The new idea is the scaling on a statistical basis of the magnetic variations to the electric field in the solar wind in order to make the new PC index independent of the local ionospheric properties and their daily and seasonal variations. The PC index concept was further developed by Vennerstrøm (1991) and Vennerstrøm et al. (1991). The development

of a PC index was recommended by IAGA in 1999 and the index was later adopted by IAGA as an international standard index on the condition that a unified procedure for the PC index calculations was defined. Unfortunately, this unification has not been accomplished yet, although a close cooperation between the Arctic and Antarctic Research Institute (AARI) responsible for the PCS index, and the Danish Meteorological Institute (DMI) formerly responsible for the PCN index, has solved most of the initial disagreements (Troshichev et al., 2006).

The relative importance of the solar wind dynamical pressure and the interplanetary geo-effective electric field for the various disturbance processes like the build-up of the current systems involved in magnetic storms and substorms is a subject of great controversy. Here, we shall specifically discuss the relations of the transpolar currents characterized by the PC index to the "external" solar wind parameters, $E_M$ and $P_{SW}$, and we shall also consider the influence of "internal" auroral substorm processes parameterized by the auroral electrojet indices, primarily the AE and AL indices.

Following the introduction in section 1, section 2 briefly outlines the high-latitude response to solar wind forcing while section 3 more specifically discusses the response in the magnetic recordings to IMF variations. Section 4 outlines the calculation procedures for the PC indices, while section 5 discusses in more detail the relations between the PC indices and the merging electric field in terms of timing and amplitude response as well as the effects of the solar wind dynamic pressure on the PC index. Section 6 discusses the relations between the PC index and various further geophysical disturbances such as auroral electrojet activity, Joule and particle heating of the upper atmosphere, and the ring current activity. Finally, there is a concluding summary section.

## 2. High-latitude response to solar wind-magnetosphere interactions

It was early recognized (e.g., Spreiter et al., 1966) that the solar wind dynamical pressure to a large extent controls the general morphology of the magnetosphere, among other, its size and shape and also affects the internal magnetic field configuration. An important parameters to characterize the impact of the solar wind on the magnetosphere is the dynamical pressure, $P_{DYN}$ :

$$P_{DYN} = D_{SW} V_{SW}^2 = M_{SW} N_{SW} V_{SW}^2 \quad (1)$$

where $V_{SW}$ is the solar wind velocity while the density, $D_{SW}$ , is a combination of solar wind number density, $N_{SW}$, and average particle mass, $M_{SW}$,. After transition through the bow shock into the magnetosheath the solar wind dynamic pressure ($P_{DYN}$) is partly converted into thermal pressure ($N_{SW}$ kT). At the magnetopause in Spreiter's model the thermal pressure from the solar wind in the magnetosheath is balanced by the internal "magnetic pressure" (i.e., $N_{SW}$ kT=$B_M^2/2\mu_o$). The magnetic field generated by the boundary currents must cancel the geomagnetic field outside the magnetopause and adds to doubling the field strength just inside the boundary.

However, the solar wind electric field is in most cases the dominant factor for the high-latitude magnetospheric electric field structures and related plasma convection processes. A useful parameter is the "merging" (or "reconnection" or "geo-effective") electric field defined by Sonnerup (1974) and Kan and Lee (1979):

$$E_M = V_{SW} B_T \sin^2(\theta/2) \quad (2)$$

This parameter is a combination of the solar wind velocity, $V_{SW}$, and the transverse component, $B_T$ , ($B_T = (B_Y^2 + B_Z^2)^{1/2}$) of the interplanetary magnetic field (IMF) in the solar wind and includes a strong dependence on the field direction represented by the polar angle $\theta$ of the transverse component of the IMF with respect to the direction of the Z-axis in a "Geocentric Solar Magnetospheric" (GSM) coordinate system (i.e., $\tan(\theta) = |B_Y|/B_Z$, $0 \le \theta \le \pi$).

The merging electric field is the optimum parameter to characterize the energy transfer from the solar wind to the magnetosphere (Akasofu, 1979). It was shown theoretically by Kan and Lee (1979) that the time dependent power, P(t), delivered by the solar wind dynamo to the Earth's magnetosphere can be expressed in terms of the merging electric field, $E_M$, (defined in Eq.2) by:

$$P(t) = E_M^2 \ell_o^2 / R \quad (3)$$

where R is the total equivalent resistance connected to the solar wind-magnetosphere dynamo. The resistance includes the dissipation processes in the reconnection region, the energy used in driving the internal magnetospheric convection and building the ring current as well as the energy dissipated in the upper atmosphere by Joule heating and particle precipitation particularly in the auroral regions. The parameter $\ell_o$ is an interaction length ( $\approx 7\ R_E$), which, when projected along geomagnetic field lines to the polar cap ionosphere, defines the width of the open polar cap. Equation (3) indicates the importance of $E_M$ to characterize the energy input although the concept is simplified and the parameters $\ell_o$ and R may not be quite well-defined or constant.

The interaction between the solar wind and the Earth's magnetosphere is sketched in Fig. 1 (from GEM Source book, 1999). The magnetosphere is delimited by magnetopause currents to provide the transition from the terrestrial magnetic field to the solar wind. In the diagram the direction of the IMF, depicted by the field lines, is assumed to be southward. In consequence, the IMF and the magnetospheric field merge at the front of the magnetosphere, where the terrestrial field is northward. The combined field reach to the ionosphere in the polar cusp region and is then dragged tailward over the polar cap and into the tail region by the plasma motion. In the middle of the tail region the neutral sheet of transverse currents separate the sunward magnetic field in the upper part of the plasma sheet from the antisunward magnetic field in the lower part of the plasma sheet.

The plasma flow just inside the magnetopause and in the northern and southern lobes at high latitudes is antisunward as in the solar wind, while the plasma motion is generally sunward at lower latitudes in the plasma sheet further inside the magnetosphere. The plasma velocity and pressure gradients close to the flanks of the magnetosphere generate the so-called "Region 1" (R1) field-aligned currents (FACs), downward to the ionosphere at the morning side, and upward from the ionosphere at the evening side. Part of the R1 currents that enter or leave the ionosphere closes across the polar cap while another part closes across the auroral oval to the "Region 2" (R2) field-aligned currents. The R2 FAC, upward at the morning side and downward at the evening side, connect to the ring current region at 4-6 Re and close through a partial ring current flowing from the morning to the evening side near equator (Iijima & Potemra, 1976a,b).

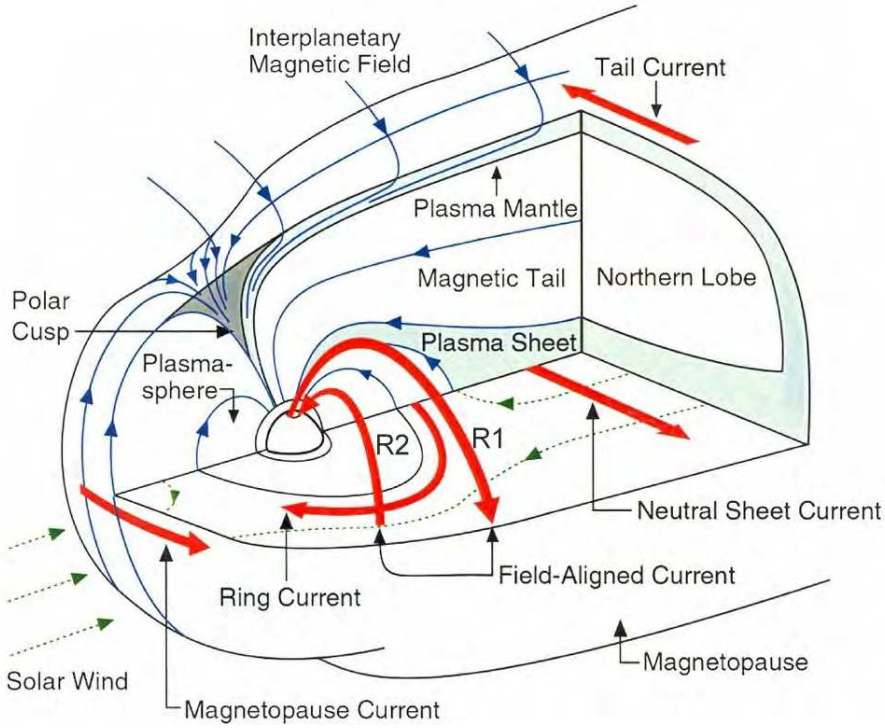


Fig. 1. Simplified sketch of magnetospheric structure (from GEM Source Book, 1999)

The polar ionospheric convection and current systems that could affect the magnetic variations measured from ground within the central polar cap could be divided into distinct categories, DP1, DP2, DP3 (or NBZ), and DP4 (or DPY) characterized by their relation to substorm activity and interplanetary magnetic field conditions (e.g., Wilhjelm et al., 1972; Friis-Christensen & Wilhjelm, 1975; Troshichev et al., 1986; Weimer et al, 2010). Each type of convection pattern comprise field-aligned currents (FAC) and horizontal Hall and Pedersen currents. The magnetic variations at ground can be assigned to a system of "equivalent currents", which in many cases will correspond to the ionospheric Hall currents that dominate the response at ground level, since the effects of the field-aligned currents and the horizontal Pedersen currents tend to cancel each other (Fukishima, 1969). The convective motion and the Hall currents are both transverse to the electric field but in opposite directions. Thus the convection patterns and the equivalent current patterns, although oppositely directed, will bear close resemblance. Both patterns are also close in shape to the equipotential contours.

The DP2 two-cell convection system comprising antisunward convection of plasma over the polar cap at all altitudes from the ionosphere up through the polar magnetosphere to the solar wind is the prevailing system except during intervals of strong northward IMF. However, the DP2 system may be modified to a greater or lesser extent by effects related to the DP1 (substorm) or/and the DP4 (DPY) convection systems. During northward IMF one or both vortices of the DP3 (NBZ) convection system could be formed at very high latitudes inside a weakened DP2 system prevailing at lower latitudes.

## 3. IMF and solar wind impact on polar geomagnetic variations

The main part, around 97%, of the geomagnetic field is generated by internal sources in the Earth's core and crust. The field from the core, the main field, has relatively slow (secular) variations in magnitude as well as in direction. The crustal remnant magnetization is constant on geological time scales. The remaining field contributions generated by external current systems and their induced counterparts in the ground are generally found by subtracting a set of base line values from the measured field components.

The external contributions can be subdivided into two fractions. One is associated with the effects of the slowly varying solar UV flux and the rather steady flow of solar wind plasma past the Earths magnetosphere during intervals with quiescent conditions. When this part, the so-called "Quiet Day" (QDC) variation, is also subtracted from the observed geomagnetic field, then the remaining field contributions are mainly related to the combination of enhanced solar wind velocities and an appreciable magnetic field in the solar wind, which may strongly influence the interaction of the solar wind flow with the Earths magnetosphere. The interaction manifests itself, among other, through enhanced ionospheric currents and associated magnetic variations in the Polar Regions.

Hourly values of the interplanetary magnetic field at the Earth's position derived from the ACE data base for the year, 2002, are shown in the top field of Fig. 2. These magnetic data are resolved in Geocentric Solar Magnetospheric (GSM) coordinates, $B_X$ (toward the Sun), $B_Y$ (perpendicular to the Earth-Sun line and to the Earth's magnetic dipole axis) and $B_Z$ (completing an orthogonal system) almost in the direction of the (negative) dipole axis. Throughout the diagrams in Fig. 2 the heavy red continuous curves depict smoothed averages.

Typical examples of polar geomagnetic observations are also presented in Fig. 2. The middle field displays the data from Thule, Greenland, located at corrected geomagnetic (CGM) latitude of $85.30^{O}$. The bottom field displays data from Vostok, Antarctica, located at corrected geomagnetic latitude of -83.58°. The thin blue traces in the diagram show hourly average values of the field resolved in the H-component (geomagnetic North), E-component (East) and Z-component (down for Thule, up for Vostok) through the year 2002.

In these data several features are noteworthy:

i. There are daily variations in all components during quiet as well as disturbed conditions judging the disturbance level from the IMF data in the top field. The main part of these variations is related to the rotation of the station beneath the more or less stationary polar cap current patterns.
ii. The polar magnetic data, particularly the E-component of the Thule observations, display small but significant steady changes through the year. These changes result from secular variations in the main field.
iii. There are low-frequency modulations on time scales from one to a few weeks seen in the interplanetary $B_X$ and $B_Y$ magnetic field components as well as in the ground-based Thule and Vostok data, most distinctly in the Z-component. These modulations are indicative of the interplanetary sector structure where the preferred field direction is either toward or away from the Sun. The associated changes in the polar magnetic field represent the so-called Svalgaard-Mansurov effect (Svalgaard, 1968; Mansurov, 1969).

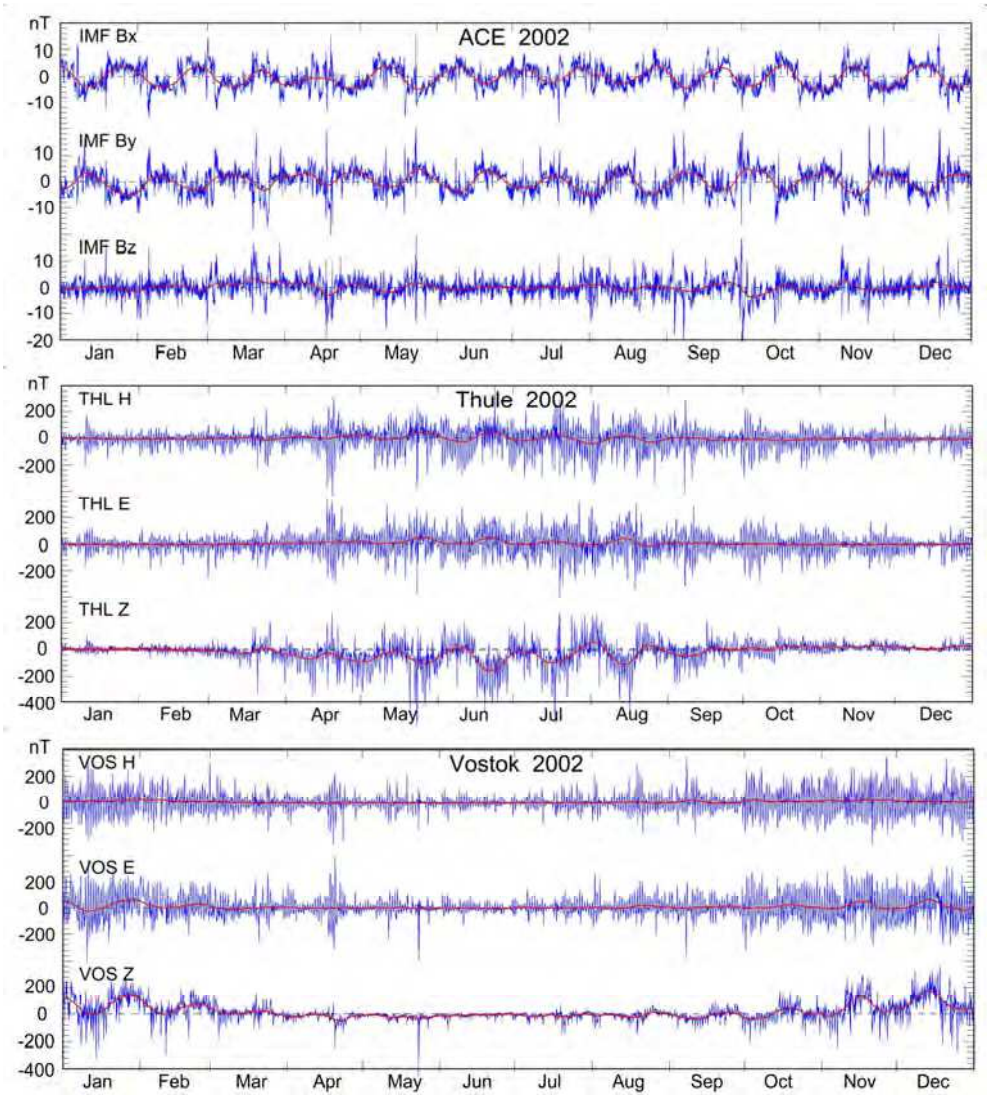


Fig. 2. ACE interplanetary magnetic field data (top) and polar geomagnetic field data from observatories in Thule, Greenland (middle), Vostok, Antarctica (bottom). Hourly values 2001.

iv. Strong high-frequency excursions, here on time scales of one to a few hours, are seen in the interplanetary data as well as in all three components of the ground-based data. In the ground-based data for Thule these excursions are strongest during the northern summer months occurring at the middle of the diagram. In the data from Vostok, correspondingly, the strongest excursions are seen in the southern summer months occurring at either ends of the diagram. The excursions on time scales from minutes to

hours observed in the solar wind and at ground in the polar cap are strongly correlated. This correlation is the fundamental basis for defining a Polar Cap (PC) index.

Basically, the Polar Cap (PC) index is defined to be a proxy for the merging electric field by assuming a DP2 (or DP2-like) convection system with antisunward plasma convection and uniform sunward Hall current across the central polar cap. It is further assumed that there is proportionality between the horizontal magnetic field variations, $\Delta F$, in the central polar cap and the merging electric field, $E_M$, and that the magnetic variations related to $E_M$ have a preferred direction with respect to the Sun-Earth direction. Thus, on a statistical basis from observations of $\Delta F$ and $E_M$:

$$\Delta F_{PROJ} = S \cdot E_M + \Delta F_I \tag{4}$$

where $\Delta F_{PROJ}$ is the projection of the magnetic disturbance vector, $\Delta F$, to the "optimum direction", that is, the direction most sensitive to the merging electric field. The parameter S (often named $\alpha$) is the "Slope", and the residual, $\Delta F_I$, (often named $\beta$) is the "Intercept" parameter, named from a visualized graphical display of $\Delta F_{PROJ}$ against $E_M$. Throughout the calculations we express magnetic fields in nT and the electric fields in mV/m.

In order to calibrate magnetic variations with respect to the merging (geo-effective) electric field we now define the PC index by the inverse relation:

$$PC = (\Delta F_{PROJ} - \Delta F_I)/S \quad (\sim E_M \text{ [in mV/m]}) \tag{5}$$

The scaling parameters, that is, the optimum direction angle, the slope and the intercept, are found from Eq. 4 by regression analysis of polar observatory geomagnetic observations against interplanetary satellite data to include daily as well as seasonal variations. This scaling serves to make the resultant PC index independent of the regular daily and seasonal variations in parameters like the ionizing solar UV flux, that are not related to the merging electric field. Furthermore, the index is also now independent of the geographical position as long as the observatory is located within the central polar cap, where the magnetic variations are mostly associated with the rather uniform transpolar electrical currents that, in turn, relate mainly to the merging electric field in the solar wind and not to auroral substorm processes.

## 4. Calculation of PC indices

The calculation of PC indices according to Eqs. (4) and (5) requires a number of steps. Firstly, the calibration constants, optimum angle, slope and intercept, must be determined from Eq. (4) using lengthy series of correlated values of the merging electric field (Eq. 2) existing in the solar wind but adjusted in timing to apply to the Polar Cap, and geomagnetic variations corrected for secular variations and quiet day variations (QDC). Then the actual magnetic variations, again corrected for secular and quiet day variations, could be used in Eq. (5) with the calibration parameters, selected from tables spanning time of day and day of year, to provide PC index values (Troshichev et al., 2006; Stauning et al., 2006).

### 4.1 Satellite observations of solar wind and IMF parameters

Data for the merging electric field in the solar wind are needed for the derivation of the scaling parameters. During the time interval from 1975 to present, where high-quality digital magnetic

data are available from Thule there are four main sources of solar wind plasma and interplanetary magnetic field data. These sources are IMP 8, Wind, Geotail, and ACE satellite data. Here we concentrate on IMP8 and ACE data for calculations of the scaling parameters, but Geotail and Wind satellite data can be used in special correlation studies since they offer further ranges of satellite positions with respect to the magnetosphere.

The IMP 8 satellite was launched 1973-10-26 into an orbit with inclination varying between 0 deg and 55 deg. Apogee and perigee were around 40 and 25 earth radii, respectively. Data are available up to June 2000. The spacecraft was located in the solar wind for 7 to 8 days of every 12.5 days orbit. Telemetry coverage has been varying between around 60 and 90%.

The ACE satellite was launched 1997-08-25 into a halo orbit about the L1 point. The satellite instruments and telemetry have provided almost 100% recovery of magnetic data and solar wind velocity data since the beginning of 1998. The satellite is still active. The main advantage of using ACE data is their regularity over the years, which are now spanning more than one full solar activity cycle. The main disadvantage of using ACE data is the large distance of around 240 Re (~1.500.000 km) from the Earth to the satellite. This large distance causes a delay of typically around 1 hour for the solar wind with its embedded magnetic field to travel from the satellite position to the encounter with the Earth's magnetosphere.

In most previous satellite-ground correlation studies IMP 8/ACE data have been referred to a fixed position at 12 Re in front of the Earth in order to provide a uniform basis. This modification is accomplished by shifting the data in time with an amount corresponding to the solar wind travel time from the actual satellite position to the GSE (=GSM) X-coordinate of the reference position assuming uniform conditions in planes perpendicular to the Sun-Earth line. For the recent analyses (Weimer & King, 2008), the satellite data have been shifted to the position of the bow shock nose (BSN). A detailed description of the shift is provided at the web site http://omniweb.gsfc.nasa.gov/.

For IMP 8 the upper limit on the X-coordinate is around 40 Re. This leaves a span for the solar wind travel from the satellite to the reference location to deal with distances between -12 Re (at $X_{GSE}$ = 0 ) and +30 Re, which with typical solar wind velocities of 350 km/sec corresponds to delays ranging between around -4 min and +10 min. For ACE the typical delay is around 60 min between solar wind observations at the satellite and the encounter of the same solar wind volume with the Earth's magnetosphere (12 Re or BSN reference position). The above-mentioned delays are just typical values. In actual cases the precise satellite position and the observed solar wind velocity were used to calculate the relevant delays. With the above outlined procedure, all the relevant solar wind field and velocity parameters have been converted into 1-min samples at the reference position. For some of the statistics we proceed to calculate 5-min sorted averages (excluding max and min values, average of rest).

From the reference position (12 Re or BSN) it takes the $E_M$ effects some time to propagate and affect processes in the central polar cap ionosphere. Precisely how the effects propagate to the polar cap ionosphere is still an open question involving magnetospheric convection processes, pressure gradients, field-aligned currents and coupling to the ionospheric potential and current systems. It is shown below that this time interval is around 20 min. Accordingly, the series of merging electric field values referenced to 12 Re or the bow shock nose should be further time-shifted by 20 min before being correlated with polar cap magnetic variations. In the further derivation of *PC* index parameters and other uses of IMF

and solar wind data we have selected to base all calculations on IMP 8 and ACE data discarding the Wind and Geotail measurements except for specialized applications.

### 4.2 Handling of geomagnetic data

It is clear from Fig. 2, particularly in the trace for the geomagnetic E-component measured at Thule, that the magnetic field related to internal sources changes slowly. For Thule these secular changes in the components amount to several tens of nT each year. In Vostok the secular changes are smaller. These changes are unrelated to solar wind and ionospheric effects and must be corrected for before PC index values are derived. Thus the baseline caused by the "internal field" contribution should be derived. During midwinter, at night hours and for very quiet conditions, the "external field" contributions are at minimum, at most a few nT. Consequently, the winter night magnetic recordings are carefully monitored in order to detect the magnetic component values during extremely quiescent conditions. For Thule, these values, considered to represent the baseline related to the "internal field" contributions, are referenced to 1. January and kept since 1973 in a yearly updated "Quiet Winter Night Level", QWNL, table. It is assumed that the baselines for the individual components, with the accuracy needed for PC calculations, vary linearly through the year such that they could be interpolated from the values at day 1 one year to day 1 the following year, or extrapolated beyond 1 January through the actual year.

The "Solar Rotation Weighted" (SRW) calculations of the "Quiet Day Curve" (QDC) at DMI are explained in Stauning (2011). The method builds on superposition of a selection of quiet segments to build a QDC for each component separately for any given day. The samples are weighted according to the variability in the horizontal component. In the superposition of quiet recordings from different days, further weight functions are applied to give preference to intervals close to the QDC day in question and to intervals where the same face of the sun is directed towards the Earth. The solar rotation weight factor takes into account the regular variations in the solar UV radiation, in the solar wind velocity and in the IMF sector structure. The procedure is fully automatic and a quality parameter (the sum of weights) is provided for each hourly QDC value to enable a warning for poorly defined QDC values. Quadratic interpolations are used to provide QDC values with finer than one hour time resolution (e.g., 1-min samples). The baseline values and the QDC values calculated for each day of the data range are now subtracted from the recorded data to provide the series of magnetic variations to be used for PC index calculations. Composite plots of baseline-corrected magnetic recordings from January and July 2002 and the QDC values for these intervals are shown in Fig. 3.

### 4.3 Optimum direction angle

Searching for a proxy based on polar magnetic disturbances to represent the solar wind merging electric field ($E_M$ = MEF = $V_{SW}$ $B_T$ $\sin^2(\theta/2)$), we may increase the correlation between the horizontal disturbance vector $\Delta F$ (corrected for the quiet daily variations) and the $E_M$ by projecting $\Delta F$ to a specific direction ("optimum direction"). In principle, this direction is perpendicular to the transpolar DP2 current. The direction is not entirely fixed in space but varies slowly with local time and season. The rotating horizontal magnetic vector is resolved in an X-component (northward in a geographical coordinate system) and a Y-component (eastward). The vertical Z-component is downward in the northern polar cap.

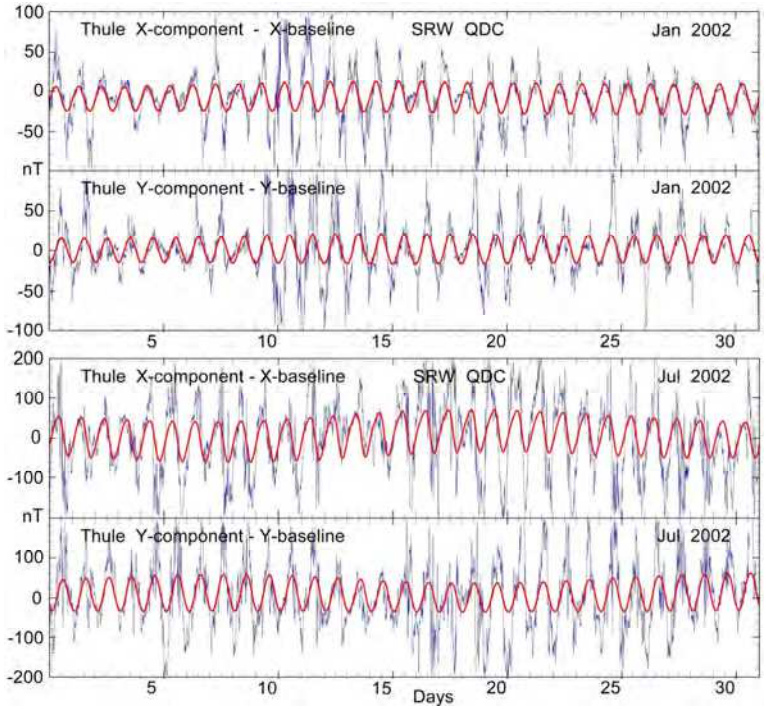


Fig. 3. Thule baseline-corrected magnetic data and QDC for X- and Y-components for January and July 2002.

For the horizontal components we first subtract from the raw data the baseline values and then the QDC values, i.e.:

$$\Delta X = ( X_{RAW} - X_{BL} ) - X_{QDC} \tag{6a}$$

$$\Delta Y = (Y_{RAW} - Y_{BL} ) - Y_{QDC} \tag{6b}$$

Here, $X_{BL}$ is the baseline value for the X-component defined yearly (every 1 January) and now adjusted to the actual day-of-year. $X_{QDC}$ is the reference QDC level provided as tables of hourly values for each day and now adjusted to the proper time. The Y-component is handled correspondingly.

Using the + sign for the southern hemisphere and the – sign for the northern, the projection of the disturbance vector ΔF to the optimum direction is given through:

$$\Delta F_{PROJ} = \Delta X \cdot \sin (V_{PROJ}) \pm \Delta Y \cdot \cos(V_{PROJ}) \tag{7}$$

where the angle $V_{PROJ}$ is defined as a function of UThr (UT time in hours) through:

$$V_{PROJ} = \text{Longitude} + \text{UThr} \cdot 15^{o} + \text{optimum direction angle (ODA)} \tag{8}$$

With this definition, the "Optimum Direction Angle" (ODA) is the angle between the dawn-dusk direction and the optimum direction for the magnetic variation vector. This angle is

also the angle between the midnight-noon direction and the transpolar equivalent current direction, which by definition is perpendicular to the related magnetic disturbance vector.

The optimum direction angle values are calculated from statistical analyses to find the maximum correlation between the geomagnetic variations measured in the polar cap and the solar wind merging electric field values derived from interplanetary spacecraft data, which have been time-shifted to apply to polar cap effects. The direction depends on observatory location and varies with day of year, and UT time of day. With this procedure we have calculated and tabulated the optimum direction angle for each UT hour of the day and each month of the year.

### 4.4 Calculations of slope and intercept

It is the general assumption that there is a linear relation between the projected polar magnetic variations, $\Delta F_{PROJ}$, and the solar wind electric field, $E_M$, and that this relation can be inverted and used to define a PC index by equivalence (cf. Eqs. 4 and 5). This relation assumes a DP2-type two-cell polar ionospheric "forward" convection, which is the most common convection mode. It applies to solar wind conditions where the interplanetary magnetic field (IMF) is either southward oriented or only weak in magnitude when northward directed. During conditions of strong northward oriented IMF a DP3 reverse convection system may develop in which the transpolar flow is sunward, while the return flow is antisunward.

With an overhead reverse current direction the magnetic deflections at ground are opposite of those of the forward convection mode. Accordingly, the projected disturbance vector may become less than the QDC level or even strongly negative. PC index values calculated during such conditions may turn out to be negative. Since the interplanetary merging electric field ($E_M$ ) by definition (Eq. 2) is always non-negative, then the concept of the PC index as a proxy for the $E_M$ breaks down. Hence, reverse convection cases must be excluded from the calculations of slope and intercept.

In a least squares fit to estimate the regression of $\Delta F_{PROJ}$ on $E_M$ from a comprehensive and representative data base, the deviations of the magnetic variations from the regression line are minimized whereby the slope, S, and the intercept parameter, $F_I$ , are derived. With this procedure we have calculated and tabulated values of the slope, S, and the intercept parameter, $\Delta F_I$ , for each UT hour of the day and each month of the year.

### 4.5 PCN, PCS and combined PC index, PCC

The PCN index for the northern polar cap is based on data from the Danish geomagnetic observatory in Thule (Qaanaaq) in Greenland while the PCS index for the southern polar cap is based on data from the Russian geomagnetic observatory in Vostok at Antarctica. Parameters for the two observatories are listed in Table 1.

| Station name | IAGA code | Geocentric Latitude | Geocentric longitude | Corr. geomag. latitude | Corr. geomag. longitude | UT at MLT noon |
|---|---|---|---|---|---|---|
| Qaanaaq | THL | 77.47 | 290.77 | 85.30 | 31.11 | 15:04 |
| Vostok | VOS | -78.46 | 106.87 | -83.58 | 54.77 | 13: 02 |

Table 1. PC geomagnetic observatories in the northern and southern polar caps. Epoch 2000

Both the PCN and the PCS indices have been calibrated with respect to the merging electric field (MEF=$E_M$) in a statistical sense. Accordingly, the two index series are also mutually equivalent in a statistical sense. However, differences may arrive as the result both of different conditions in the two polar caps (e.g., different solar illumination) and of different response to forcing from the solar wind as well as different response to substorms. Such differences have the potential for interesting studies (e.g., Lukianova et al., 2002).

Another possible application of the two PC index series uses the possibility to define "summer" or "winter" PC index series based alternating on either PCN or PCS depending on local season. Thereby characteristic seasonal variations may emerge more clearly than otherwise by using one or the other hemispherical index series.

A further possibility is the combination of the two index series into one (Stauning, 2007). In the most common two-cell forward convection cases the projected magnetic variations and the PC index values are positive. However, with overhead reverse convection flow during NBZ conditions the magnetic deflections are opposite to those of the forward convection mode. Accordingly, the projected disturbance vector may become less than the QDC level or even strongly negative. PC index values calculated during such conditions may turn out to be negative. Since the interplanetary merging electric field by definition is always non-negative (cf. Eq. 2) then the concept of the PC index as a proxy for $E_M$ breaks down.

Such cases of reverse convection and large negative PC index values are, by far, most common at daytime in the summer season. In these cases the forward convection mode may still prevail at the local winter season in the opposite polar cap and the PC index values derived there may be small but still positive like $E_M$. A simple way to accomplish a combined PC index would be to calculate the plain average values of the PCN and PCS data series. However, the problem with large negative PC index values in one hemisphere speaks for constructing a combined PC index (PCC) from non-negative values only. Accordingly:

$$PCC = [(PCN \text{ if } >0 \text{ or else zero}) + (PCS \text{ if } >0 \text{ or else zero})]/2 \quad (9)$$

This option was tested in Stauning (2007) who examined the correlation between $E_M$ and PCN, PCS, and the new PCC values, respectively. From this work, Fig. 4 presents hourly average values of $E_M$, PCN, PCS and PCC index values through the year 2000. The top field displays $E_M$ values calculated according to Eq.2 from ACE satellite measurements of the interplanetary magnetic field and the solar wind velocity. The parameters measured at the ACE satellite have been shifted to apply to polar cap effects. The second and third fields from the top present PCN and PCS values using identical procedures in the calculation of the two index series. The bottom field presents the PCC index values derived from using Eq. 9.

Fig. 4 indicates a close similarity between the enhancements in $E_M$ and the positive enhancements in PCN and PCS. These enhancements are, of course, also seen in the combined PC index, PCC. Further, the occurrences of negative PCN and PCS index values, preferably during the local summer seasons in the two hemispheres (May-August for PCN, November-February for PCS) should be noted. These events have no proportional (i.e., strongly negative) counterpart in $E_M$ values. The relevant merging electric field values are just small at these times. The new PCC index displays the positive enhancements corresponding to the larger values of $E_M$ and, by its definition, no negative values even during NBZ conditions.

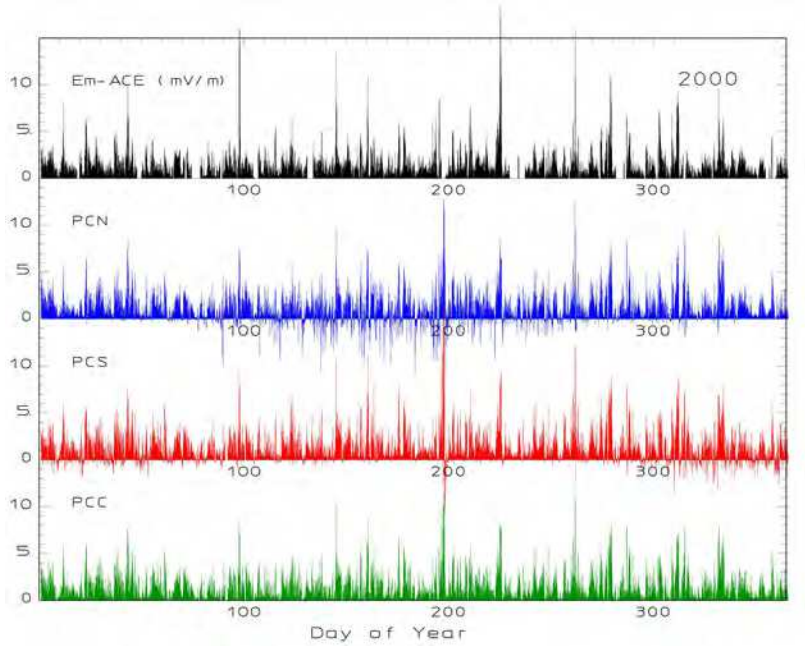


Fig. 4. Hourly averages calculated from 5 minute values of the merging electric field (top), Polar Cap PCN and PCS indices (middle) and new PCC index (bottom) through 2000.

## 5. Further relations of PC indices to solar wind parameters

The definition and the calculation of polar cap indices are based on an assumed linear dependence (cf. Eqs. 4 and 5) on the merging electric field, $E_M$ (cf. Eq. 2). However, there are a number of additional effects, which could be of importance for various applications of the indices. Such effects, which to some extent violate the premises, include:

i. Delayed PC index response to variations in the merging electric field.
ii. Non-linear effects such as saturation of PC index values at high levels.
iii. Response in the PC index to variations in the IMF Bx component not included in $E_M$.
iv. PC index response to solar wind dynamic pressure variations.

It is important to be aware of these modifications of the simple straight relations between $E_M$ and the PC indices in order to recognize their signatures or consider whether they could deteriorate analyses of the relations between the PC indices and further terrestrial parameters.

### 5.1 Timing of PC index variations at changes in the merging electric field

When a change in the merging electric field, $E_M$, hits the magnetosphere then it takes some time for the polar cap convection pattern, and thus the PC index, to adjust to the new level. The timing issue could be analyzed in two ways. First, one could look for distinct variations, for instance, step-like changes in $E_M$, which could easily be recognized in the PC indices. Then

the relative timing between Em and PC would provide the desired relation. Another approach would be to investigate statistically the correlation between $E_M$ and PC index values with a variable delay in order to disclose the optimum value. We shall proceed both ways.

The top field of Fig. 5a displays a plot of superimposed traces of step-like varying $E_M$. The data have been shifted to a position of 12 Re in front of the magnetosphere (close to the average position of the bow shock nose). The individual traces have been positioned such that the positive step from a low to a high value occurs at relative timing T=0. The bottom field of Fig. 5a displays the corresponding variations in PCN. The heavy traces in the two plots mark the average variation.

It is easy to see the sudden step in the average $E_M$ trace (top field) from close to zero up to around 2.5 mV/m. The average PCN index values in the bottom field display a gradual change from almost zero and up to 2.5 units, where it levels with the value of $E_M$. The change in PCN appears to start 9-10 min after the step in $E_M$. The average PCN index values reach half the final level at around 20 min after the $E_M$ step, while it takes 30-40 min to reach the final level.

The corresponding variations at a negative step in $E_M$ are displayed in Fig. 5b. In the upper field a number of step-like varying Em traces have been superposed with the step placed at relative timing T=0. From the average variations in the corresponding PCN index values it is seen that the change starts around 10 min later than the step in $E_M$. The average PCN value reaches half the level prevailing before the change at around 20 min after the negative $E_M$ step while it takes around 50 min to reach the final low level.

In summary, following a positive or negative step-like change in the merging electric field impinging on the front of the magnetosphere it takes around 10 min before the change is sensed and the PC index starts to change. At around 20 min after the $E_M$ step the PC index has reached half the final level, while it takes 40-50 min before the change is completed. The positive steps in $E_M$ propagate a little faster to affect the PC index than the negative steps.

The analysis of corresponding features based on a larger and more general selection of data is presented in Fig. 6. For the epoch from 1990 to 1999, PCN data have been plotted against $E_M$ in such diagrams with variable delays from 0 to 30 min in steps of 5 min. The IMP8 satellite data were selected for this study because of the proximity of the satellite to the magnetosphere whereby the uncertainty in the time-shift is minimized (compared, e.g., to ACE or Wind data). At each step the linear correlation coefficient, RX, was calculated along with the parameters S0 (average deviation), S1 (absolute deviation), and S2 (standard deviation). NX is the total no. of samples. The number of samples in each bin of 2 mV/m in $E_M$ is indicated by the size of the large dots and the standard deviation is indicated by the bars. The example shown here uses a delay of 20 min. From the values of RX at different delays, the optimum delay was estimated to be 18 min. At this delay the correlation coefficient was found to be RX=0.748.

A different representation of the correlation between PCN and $E_M$ is displayed in Table 2. Here, the PCN data and IMP8 $E_M$ data through 1990 to 1999 are again correlated. The data have been divided in selections based on the values of the bow shock nose distance, BSN-X, supplied with the satellite data. In addition to confirming that the delay from bow shock nose to polar cap is around 20 min, the correlation study presents further details specified in Table 2.

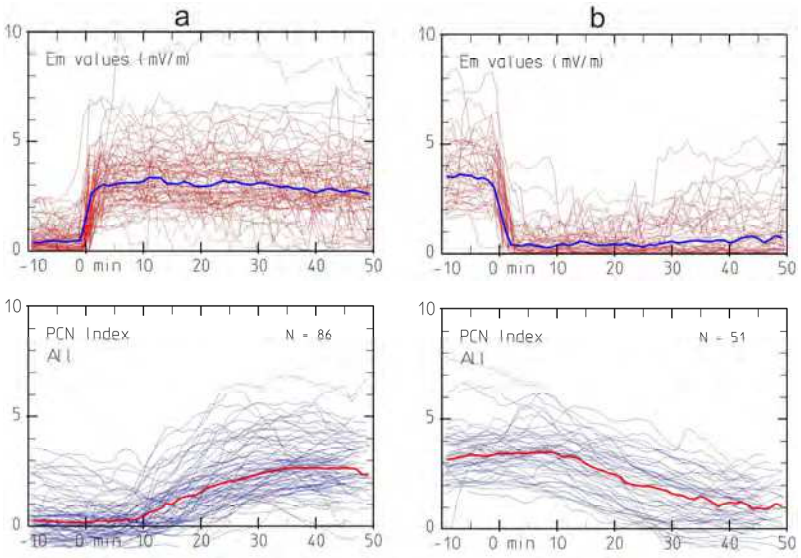


Fig. 5. PCN index variations at steps in the merging electric field at 12 Re.

| BSN-X | 8 | 9 | 10 | 11 | 12 | 13 | 14 | 15 | 16 | Re |
|---|---|---|---|---|---|---|---|---|---|---|
| NX | 397 | 2082 | 9401 | 31068 | 75318 | 87184 | 45806 | 12568 | 3136 | |
| RXmax | 0.45 | 0.59 | 0.71 | 0.74 | 0.70 | 0.69 | 0.69 | 0.70 | 0.72 | |
| DTm | 12.3 | 15.5 | 16.3 | 17.2 | 17.4 | 18.8 | 20.9 | 23.2 | 27.4 | min |
| $E_M$ av | 7.7 | 4.6 | 2.7 | 1.7 | 1.2 | 0.9 | 0.7 | 0.7 | 0.7 | mV/m |
| PCNav | 6.3 | 4.2 | 2.4 | 1.7 | 1.2 | 0.8 | 0.6 | 0.6 | 0.6 | |

Table 2. Results from correlation of PCN with values of $E_M$ at bow shock nose (BSN).

From Table 2 it is clear that for the majority of cases (90%) the BSN distances range between 11 and 15 Re, which is close to the X=12 Re used as a reference position in other analyses. It is also seen that the delay, generally, decreases with decreasing BSN distance. The decreases are larger than the reduction by 17 sec for each 1 Re decrement in distance, which is the time lapse for a typical solar wind speed of 400 km/s. The reduced correlation for the stronger cases (low BSN-X) could indicate that the strongly reduced travel time relies on the mixing of different propagation mechanisms, for instance, effects from accompanying solar wind dynamical pressure enhancements that propagate faster to the Earth than the $E_M$ -associated effects.

Another remarkable feature is the close relation between $E_M$ and PCN for the different ranges of BSN-X. It could be expected that the bow shock moves closer to the Earth when the solar wind is intense, that is, for cases of high solar wind speed and strong, southward IMF in which case the merging electric fields are enhanced. However, it is noteworthy that the average PCN index for each BSN-X interval corresponds closely to the average $E_M$ value except for the highest levels where some saturation of PCN is evident.

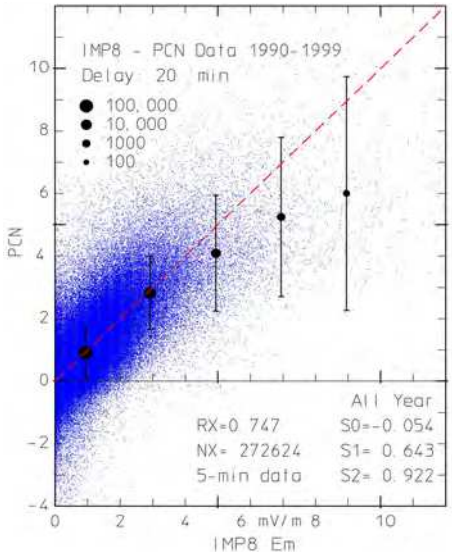


Fig. 6. Correlation scatter plot between $E_M$ at BSN and PCN for 20 min delay.

### 5.2 PC saturation effects

At high levels of the solar wind forcing, saturation effects are found in many terrestrial parameters, for instance in the polar cap potentials, in the convection velocities, and the cross-polar cap dimension, or in the length of the reconnection line. Borovsky et al. (2009) list 9 different models to explain polar cap potential saturation.

A relevant question is now whether the polar cap indices just reflect the general saturation in the magnetospheric response to strong solar wind forcing or have saturation patterns different from other geophysical disturbance phenomena. Fig, 7 displays in a scatter plot the relations between the combined PCC index and the merging electric field. The data base has been constrained to intervals of 4 days through each of 82 geomagnetic storm intervals (Dst<-100) from the epoch 1995-2005 in order to focus on the strong events with large values of the PC indices. The PCC indices have been preferred over the hemispheric PCN or PCS indices since possible saturation effects are globally extended. From the scatter plot in Fig. 7 the saturation effect is evident. The dotted curve included for reference represents the simple saturation model:

$$PCC = E_M \Big/ \sqrt{\left(1 + \left(E_M / E_0\right)^2\right)} \tag{10}$$

The asymptotic electric field value used here is: $E_0$=10.5 mV/m. The fit to the actual average PCC index values is quite good. Hence, this saturation model could serve to provide a basis for comparison of saturation in the PC index data with saturation effects in further parameters. The model (Eq. 10) might even provide some guidance in a discussion of possible saturation mechanisms.

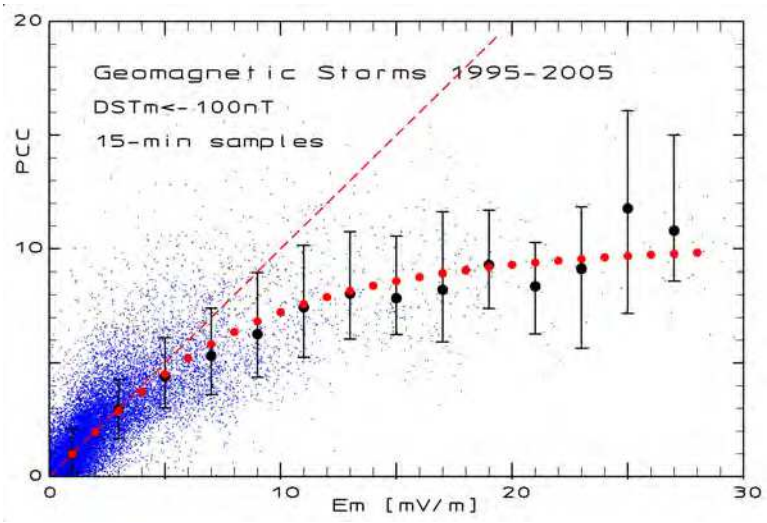


Fig. 7. PCC indices vs. related merging electric field values for all major magnetic storms (Dst<-100 nT) during 1995-2005.

The saturation effect in the PC index may also be seen as a limitation in the response to large values of the IMF Bz parameter. This is illustrated in Fig. 8. The figure displays in a scatter plot the ratio of PCN over $E_M$ as a function of the IMF Bz component. The heavy dots mark the average values within intervals of 2 nT in the Bz component. The Bz component is already included in the expression for $E_M$ (cf. Eq. 2). Ideally, the points should thus be positioned close to and symmetrically around the horizontal dashed line, which indicate a ratio of unity, and should not show any systematic dependence on the IMF Bz (or any other) component.

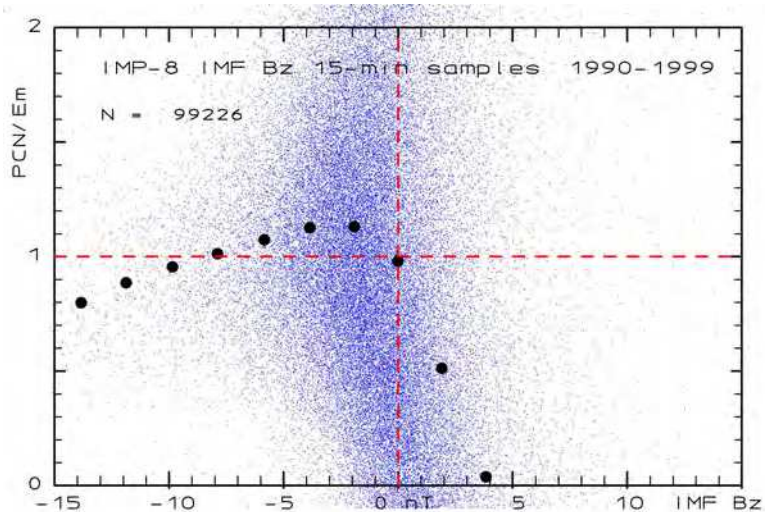


Fig. 8. Scatter plot of the ratio PCN/$E_M$ versus IMF Bz through the epoch 1995-1999.

The left half of the plot displays the ratio PCN/$E_M$ for negative values of the IMF Bz component (southward IMF). The ratio increases from 1.0 at IMF Bz ~ 0 to values between 1.00 and max. 1.13 for IMF Bz values between 0 and -8 nT. Starting from the max. level at an IMF Bz level at around -4 nT, the ratio systematically decreases in an almost linear trend to smaller values ending here at a ratio of 0.8 for IMF Bz ~ -15 nT. This systematic behaviour may – like the above saturation model – provide some guidance to the saturation mechanism.

The right part of Fig. 8 displays the ratio PCN/$E_M$ for positive values of the IMF Bz component (northward IMF). From an average value of this ratio close to unity at IMF Bz ~ 0 the ratio rapidly decreases to zero at IMF Bz ~ +4 nT and thereafter reaches large negative values since the PCN values tend to become negative while the $E_M$ values approach zero in consequence of the IMF direction getting close to due northward in some cases (cf. Eq.2).

### 5.3 Effects from the IMF Bx component on PC index values

The large-scale systematic variations in the IMF Bx component define the sector structure in the solar wind. The Bx component is positive when the IMF is pointing toward the Sun in "toward" sectors and negative in "away" sectors (Svalgaard, 1968, 1972, 1973; Mansurov, 1969). The IMF Bx component is not included in the expression for the merging electric field (Eq. 2). Hence the scaling of polar magnetic variations to construct a polar cap index is assumed to be independent of this component.

Fig. 9 displays the ratio of PCN over $E_M$ value plotted against the IMF Bx value. The scatter plot has the same format as the plot displayed in Fig. 8. The heavy dots indicate average values of the ratio PCN/ $E_M$ through intervals of 2 nT in the Bx component. These values are all within 0.9 to 1.1, that is, close to unity through most of the displayed IMF Bx range from -15 to + 15 nT . Ideally, the average value of ratio PCN/ $E_M$ should be close to unity regardless of the IMF Bx value. Thus, Fig. 9 provides a confirmation that the IMF Bx component has little influence on the PC values.

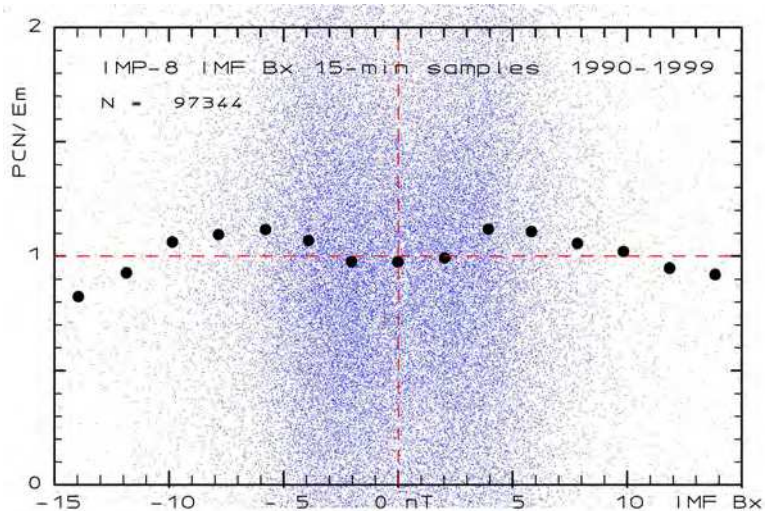


Fig. 9. Scatter plot of the ratio PCN/$E_M$ versus IMF Bx

### 5.4 Effects from variation in the solar wind dynamic pressure on the PC index

The dynamic pressure in the solar wind (cf. Eq. 1) has profound influence on the general morphology of the magnetosphere. The pressure balance at the magnetopause is an essential factor for determining the dimensions of the magnetosphere (e.g., Spreiter et al., 1966; Shue et al., 1997) and for the location of the bow shock as well (e.g., Farris & Russell, 1994). Furthermore, the solar wind dynamic pressure strongly affects the width of the auroral oval causing auroral activity to expand equatorward during intervals of enhanced pressure (Newell & Meng, 1994). However, the solar wind dynamic pressure and its variations have relatively small effects on the polar cap index compared to the effects of the merging electric field and its variations.

The PC index variations with solar wind dynamic pressure could be divided into 3 types comprising effects of different steady levels, gradual changes, and fast (impulsive) variations, respectively. The sample duration and averaging procedures should be selected accordingly. The variations in the PC index level with solar wind dynamic pressure level are illustrated in Fig. 10. The diagram is based on 15-min average values of the combined PCC index, the solar wind merging electric field ($E_M$), and the dynamic pressure ($P_{SW}$) for a series of 82 selected magnetic storm intervals during 1995-2005. Each interval comprises 4 days of which the first includes the storm onset. This selection holds a fair amount of enhanced parameter values. Each of the small points displays the ratio of PCC over the $E_M$ value (vertical axis) against the dynamic pressure (horizontal axis). The horizontal dashed line reflects the "ideal" unity ratio between PCC and $E_M$. The large "dots" indicate average values of the ratio of PCC over $E_M$ for each interval of width equal to 2 nPa in dynamic pressure. The error bars represent the 68% "standard deviation" range for the distribution of points above and below the average values.

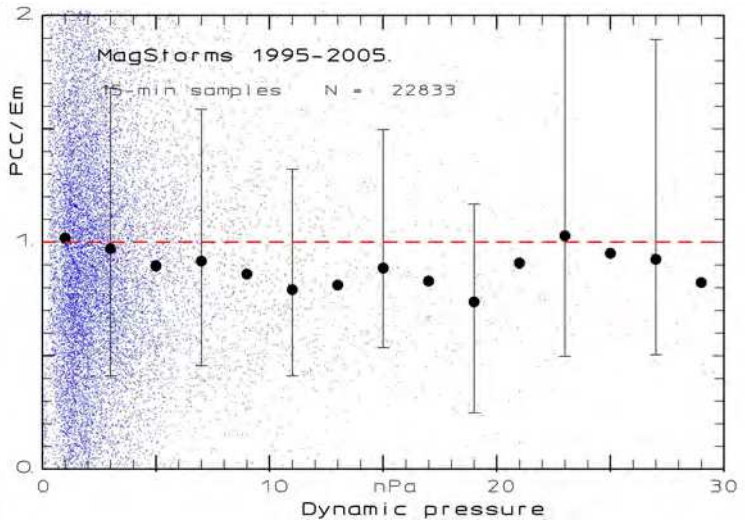


Fig. 10. Effects of varying solar wind dynamic pressure level on the PCC/Em ratio.

Like seen in other scatter plots, the scatter of points in Fig. 10 is quite large. However, it is readily seen that the average ratio of the PCC index over the merging electric field is very

close to unity for the bulk of data points representing small and moderate levels of the dynamic pressure up to around 2 nPa. For levels of the dynamic pressure from 2 up to around 10 nPa the PCC index is less than the corresponding $E_M$ value. For still larger values of $P_{SW}$ above 10 nPa the ratio of PCC over $E_M$ is again close to unity but the scatter increases due, among other, to the sparse statistics. Accordingly, through the wide range displayed in Fig. 10 the steady level of the solar wind dynamic pressure has little effect on the polar cap index values.

The relation of the PC index values to gradually changing solar wind dynamic pressure conditions is displayed in Figure 11. The solar wind pressure values used in the figure are 5-min averages of the slope of the pressure variations with time. The solar wind data have been time shifted to apply to the polar cap (cf. section 5.1). The selection of data used to determine the relation of PCC/$E_M$ to the time derivative in the solar wind dynamic pressure is the same set of storm intervals as used previously. The PC index values used in Fig. 11 are 5 min averages of the combined PCC index.

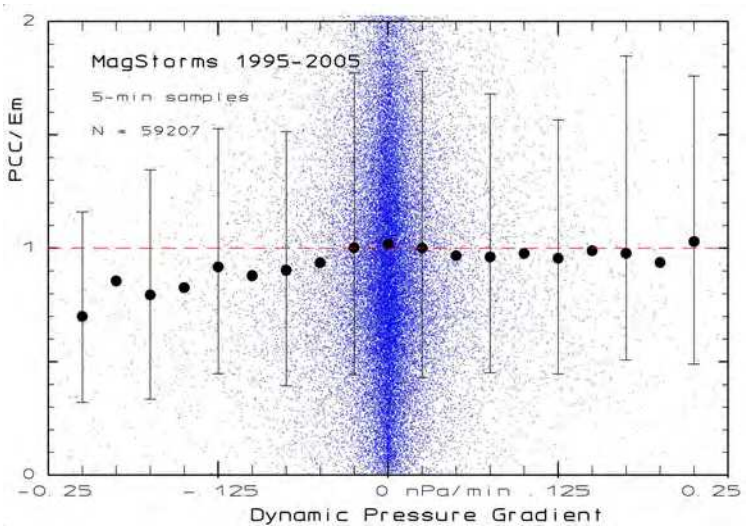


Fig. 11. Effects of dynamic pressure gradient on the ratio of PCC over $E_M$.

The large dots depict averages of all data samples within each interval of width equal to 0.025 nPa/min. For every other dot error bars have been drawn to indicate the 68% range for values above and below the average value. The average ratio of PCC to $E_M$ (in mV/m) should be close to unity. This is clearly the case for the bulk of data points with time derivative values close to zero or positive. For large negative values of the time derivative the average ratio of PCC over $E_M$ values is less than unity. The effects on the ratio PCC/ $E_M$ and thus on the PC index is fairly small within the range of gradient values displayed in Fig. 11.

The effects on the Polar Cap index of sudden (shock-like) pressure variations are depicted in Fig. 12. The top field displays the dynamical pressure variations referred to the reference position (12 Re). Each of the PCN index traces in the bottom field displays a sequence of an

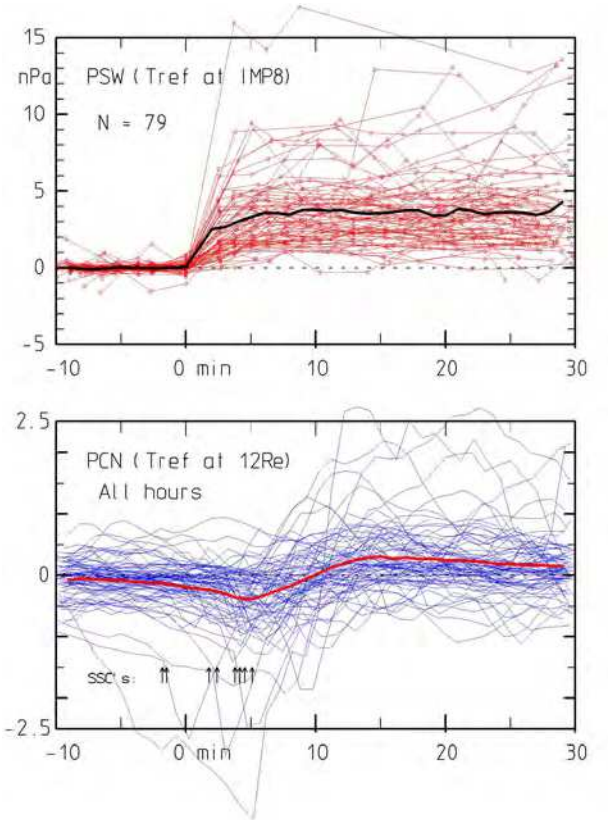


Fig. 12. PCN variations at solar wind PSW steps.

initial negative impulse followed by a positive enhancement in the index value (e.g., Lukianova, 2003; Huang, 2005; Stauning & Troshichev, 2008). The negative peak in the PC index occurs within 2-10 min following the pressure step referred to the reference position at 12 Re in front of the Earth. The width of the negative pulse is typically 3-5 min and the amplitude is around -0.5 to -1.0 units in the PC index. The positive pulse, typically, has a width of 10-20 min and amplitude of 0.5 to 1.0 units. The peak positive amplitude is typically reached ~15 - 20 min after the pressure step impacts at 12 Re. The timing implies that the pressure effects propagate from the reference position (12 Re) to the central polar cap in only a couple of minutes. This is much faster than the propagation of effects related to the $E_M$ and thus suggests different propagations processes (e.g., Araki, 1994; Stauning and Troshichev, 2008).

In summary, the PC index variations with varying level of the solar wind dynamic pressure and with impulsive variations are usually limited to range between – 0.5 and + 1.0 units. The variations at impulsive pressure enhancements could in rare cases amount to a couple of units, which is still fairly modest compared to potential variations with the merging electric field (cf. Fig. 7). The response time for the initial negative pulse in the PC index is a few minutes while the positive trailing impulse develops in 10-15 min suggesting

propagation modes different from the usual FAC and convection-based timing of variations in the PC index values with varying merging electric fields.

## 6. Relations of the polar cap indices to further geophysical disturbance phenomena

The solar wind flow past the magnetosphere generates a cross-magnetosphere electric field along the magnetopause. This field may feed large-scale convection and current systems in the magnetosphere, particularly during southward IMF conditions, and is partly mapped down to create the potential distribution in the polar cap ionosphere, which in turn generate the ionospheric currents responsible for the magnetic variations transformed into the polar cap indices.

Thus, the polar cap indices could be considered to be indicators of the power conveyed from the solar wind to the Earth's magnetosphere and ionosphere. The energy extracted from the solar wind is used to power, among others, the transpolar current and convection systems, the auroral electrojets, the Joule and particle heating of the thermosphere, and the ring currents. Hence, close relations between the polar cap indices and these disturbance phenomena could be expected.

Fig. 13 presents an example case of solar wind and geophysical parameters for a geomagnetic storm event on 12 Sept. 1999. The case has been selected to display data from the three satellites, ACE, Wind and IMP8, which were simultaneously in operation during the event. The ACE and Wind magnetic field and plasma data are displayed in the upper two fields. The traces are plotted in different colours and given different marks. In the next lower fields the merging electric fields and the dynamic pressure based on data from all three satellites have been plotted. The three lower fields display the auroral activity characterized by the AL and AE indices, the ring current intensity characterized by the SYM, ASY, and Dst indices, and the polar cap currents characterized by the PCN, PCS, and PCC indices. The average $E_M$ (MEF) and Psw values have been plotted in the bottom field for reference.

The onset of activity at ground level is indicated by the arrow marked "SSC" (Storm Sudden Commencement) at around 04 UT. During the next ~ 6 hours the Earth was hit by a cloud of enhanced solar wind density causing a strong increase in the dynamical pressure (middle field). This increase, replotted in the bottom field, had no marked influence on the PC indices and also little influence on the auroral electrojet and the ring current indices. At 09 UT the IMF Bz turned southward and the merging electric field increases strongly. This time the PC indices increased markedly and subsequently the PC indices track $E_M$ quite close, and the AE and AL traces indicate strong auroral activity. In the following sections the relations between the polar cap indices and further geophysical disturbances are discussed.

### 6.1 PC indices and polar cap potentials

The cross polar cap potential difference, $\Phi_{PC}$, is an important parameter to characterize polar cap potentials. This parameter could be investigated by radars, for instance the SuperDarn backscatter radar system (Greenwald et al., 1995), or by direct measurement of the electric field from satellites traversing the polar cap (e.g., Reiff et al., 1981; Rich and Hairston, 1994; Boyle et al., 1997; Hairston et al., 1998).

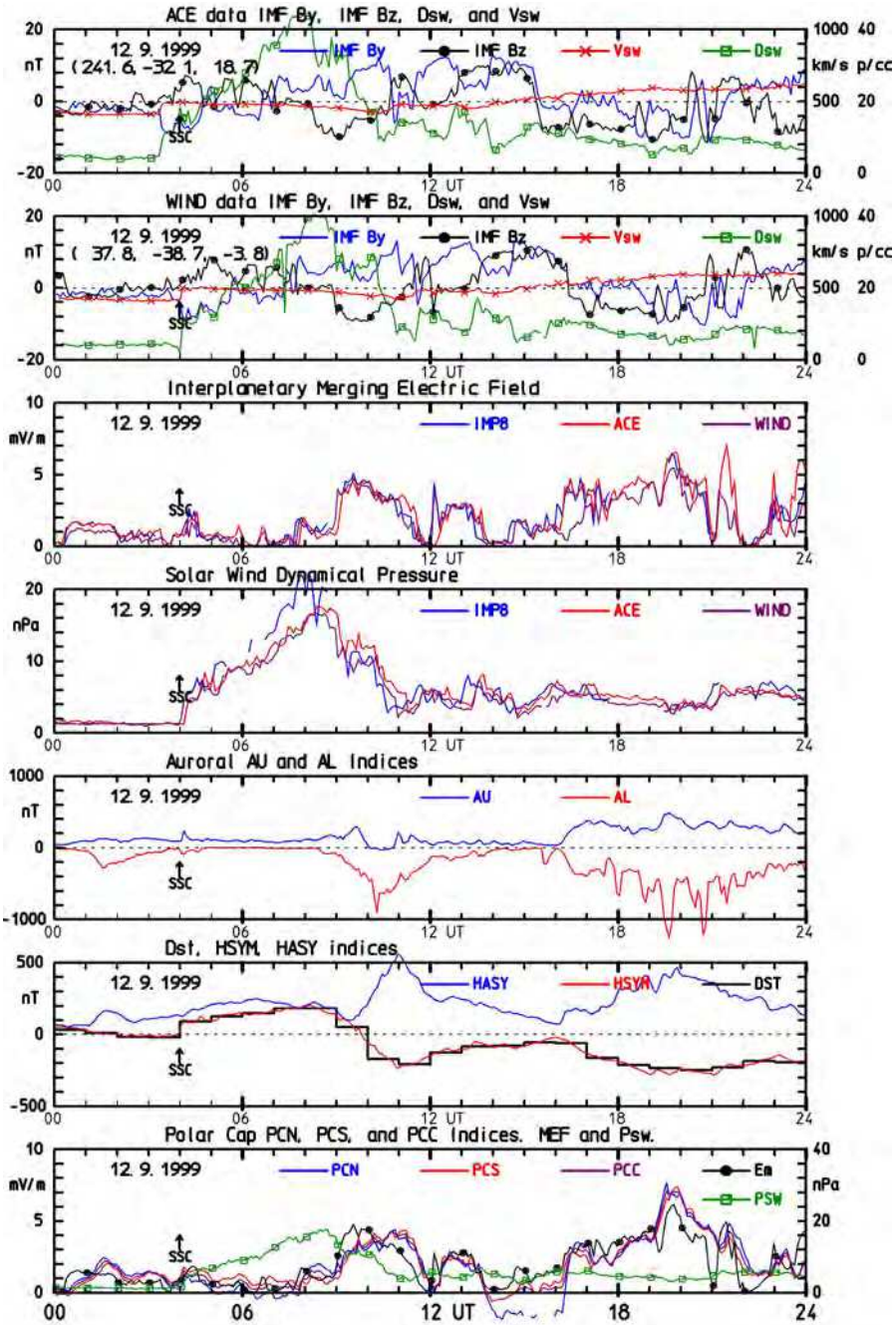


Fig. 13. Example plot of solar wind data from ACE, Wind, and IMP8, and indices for geophysical disturbances, viz. auroral electrojet, ring current, and polar cap currents.

Based on DMSP measurements, comprehensive studies by Boyle et al. (1997) suggest an empirical relation between solar wind parameters, B, $V_{SW}$, and the IMF clock angle θ, and the cross polar cap potential drop, $\Phi_{PC}$ , of the form:

$$\Phi_{PC} = 10^{-4}\, V_{SW}^2 + 11.7\, B \sin^3(\theta/2)\ [\mathrm{kV}] \tag{11}$$

Unfortunately, most of the observations relate to quiet or moderately disturbed conditions only. Thus, there were few measurements of $\Phi_{PC}$ beyond 100 kV. Hence, the expression does not provide the saturation effects observed during strongly disturbed conditions.

Further developments of empirical relations by Siscoe et al. (2002) provide relations where the height-integrated Pedersen ionospheric conductivities, assumed to be uniform across the polar cap, are included. A problem here is whether to use northern and southern hemisphere conductivities for northern and southern passes, respectively, or to use composite conductivities since the two polar caps are electrically coupled.

Hairston et al. (2005) studied specifically the saturation effects seen during strong magnetic storms. They observed that the cross polar cap potential rarely exceeded 200 kV and only in exceptional cases reached up to 250 kV. The "turn-over" from the non-saturable relation (Eq. 11) from Boyle et al. (1997) and the saturated range would occur at solar wind merging electric field ($E_M$) values between 4 and 8 mV/m.

This is also the range of $E_M$ values where the polar cap indices start to show substantial saturation effects. Interestingly, the potential data presented in Fig. 10 of Hairston et al. (2005) could well be represented by an expression similar to the above Eq. 10. Their Fig. 10 displays the cross polar cap potential drop in a scatter plot (50 points) against the merging electric field in the solar wind ranging from 0 to 40 mV/m. On basis of these data and the PCC values depicted in Fig. 7 and Eq. 10 here, the relation between the polar cap index, PCC, and the potential would read:

$$\Phi_{PC} \approx 20\ \mathrm{PCC} + 15\ [\mathrm{kV}] \tag{12}$$

The relations between polar cap index and cross polar cap diameter and voltage was investigated by Troshichev et al. (1996). They conclude that the cross polar cap voltage and radius could be expressed by:

$$\Phi_{PC} \approx 19.35\ \mathrm{PC} + 8.78\ [\mathrm{kV}] \tag{13}$$

$$\mathrm{R(morning)} = -.12\ \mathrm{PC}^2 + 2.5\ \mathrm{PC} + 11.0\ [\mathrm{deg}] \tag{14a}$$

$$\mathrm{R(evening)} = -.20\ \mathrm{PC}^2 + 3.0\ \mathrm{PC} + 12.5\ [\mathrm{deg}] \tag{14b}$$

Their expression for $\Phi_{PC}$ (Eq. 13) is very close to the above expression (Eq. 12) deduced from the observations reported by Hairston et al. (2005). Their expressions shown here in Eqs. 14a,b for the polar cap radius (angular distance from the pole) show the non-linear enlarging of the open polar cap with increasing values of the PC index.

In the analyses by Troshichev et al. (2000) they derive a non-linear expression for the average ionospheric electric field in polar regions:

$$E_{PC} = 9.29 + 3.76\ \mathrm{PC} - 0.11\ \mathrm{PC}^2\ [\mathrm{mV/m}] \tag{15}$$

For the cross polar cap potential difference, the nonlinear quadratic reduction of the electric field strength is counteracted by the expansion of the polar cap radius. For a moderately strong event the polar cap index could typically have a magnitude PC = 5. In that case the radius R ≈ 21.5° and electric field E ≈ 25.3 mV/m would give a cross polar cap voltage $\Phi_{PC}$ ≈ 121 kV, not so different from the results from Eq. 12 ($\Phi_{PC}$ ≈ 115 kV) or Eq. 13 ($\Phi_{PC}$ ≈ 106 kV).

Based on SuperDARN radar measurements Fiori et al. (2009) derived a similar relation between $\Phi_{PC}$ and the PCN index:

$$\Phi_{PC} \approx 35 + 12\ PCN\ [kV] \tag{16}$$

Their values of the cross polar cap voltage are somewhat smaller than those derived from the above expressions, Eqs. 12 and 13. However, the linear (non-saturated) relation between the cross polar cap voltages and the PC indices is maintained.

In summary, the cross polar cap potentials are linearly related to the PC index values, notably to the PCC indices, which reflect the global situation more reliably than the hemispherical indices. The ionospheric electric fields in the polar cap display non-linear saturation effects also in relation to the polar cap index, but for the cross polar cap voltages these effects are to some degree counteracted by the expansion of the polar cap during strong events to result in a linear relation between $\Phi_{PC}$ and the PC index.

### 6.2 PC indices and the auroral electrojets

The Auroral Electrojet indices were introduced by Sugiura and Davis (1966) to measure the over-all electrojet activity in the auroral zone. Index values are based on magnetic data from a number of observatories, usually between 8 and 12, located in the auroral zone. AE index values are derived as the differences over the array of observatories between the upper envelope (AU) and the lower envelope (AL) for superposed variations in the horizontal (H) components. 1-min AU/AL/AE index values scaled in nT are derived and made available by WDC-C2 (Kyoto). AU index values are mostly related to the eastward electrojet in the post-noon sector. The AL index values are most often dominated by contributions from the westward auroral electrojet currents in the morning and midnight sectors. The westward electrojet currents are strongly intensified during substorm activity. Furthermore, substorms are effective in generating intense radiation of energetic auroral particles that, in turn, precipitate to produce increased upper atmospheric electron densities. The resulting increases in ionospheric conductivities in the auroral regions, generally, further enhance the electrojet currents.

Auroral activities (e.g., substorms) are linked to the effects of the solar wind on the magnetosphere. The primary parameter in the solar wind is the merging electric field, $E_M$, but the dynamic pressure, Psw, also plays a role mainly for the position and width of the electrojet regions. The polar cap magnetic activity characterized by the PC indices could be considered representative of the input power from the solar wind to the magnetospheric processes driving auroral activities. Thus the auroral and polar cap activity levels must be related.

The correlation coefficients between the PCN or PCS indices and the AE index were calculated by Troshichev et al. (2007) for each UT hour through 1998 to 2001. An example of

the results is displayed in Fig. 14. The correlation is best at local winter where it would range between 0.80 and 0.85. During local summer the correlation is lower and ranges between 0.7 and 0.75. The results displayed in Fig. 14 also illustrate the solar cycle dependency. The correlation coefficients for PCN and PCS against AE are generally higher by 0.05-0.10 during solar minimum year (1998) than during solar maximum years (1999-2001).

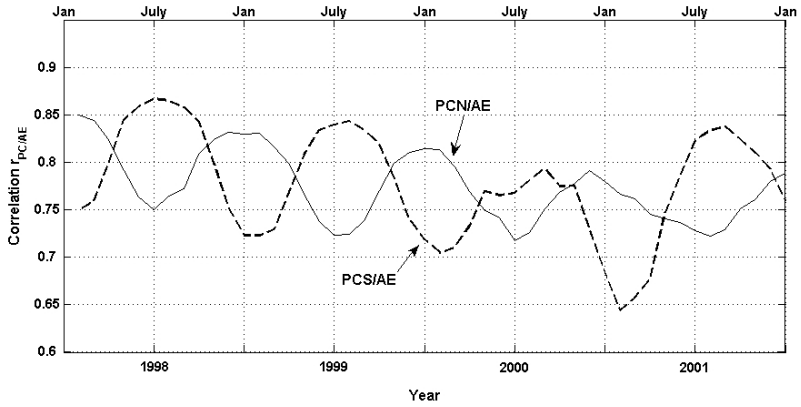


Fig. 14. Seasonal and solar cycle variations of the AE – PC correlations. (from Troshichev et al., 2007)

Another example from a recent correlation study is presented in Fig. 15. Here, values of the auroral electrojet index, AE, are plotted against corresponding values of the combined polar cap index, PCC, using a delay of 5 min. (PCC changes first). Note, that the correlation coefficient, R=0.816, for the full year is considerably higher than the above coefficients based on the individual PCN or PCS indices. Also note that the average AE indices show little indication of saturation (but larger spread) up to PCC levels of ~ 9.

The timing between sudden changes in the solar wind conditions and related changes in the polar cap and, for instance, the onset of auroral substorms as indicated by a sudden negative excursion in the AL index or a sudden increase in the AE index, was analyzed by Janzhura et al. (2007). They investigated isolated substorm events where the growth phase and the onset could be distinctly identified and related to the timing and magnitude of an increase in the PC indices caused by a gradual increase in the solar wind electric field, $E_M$. They found that when the $E_M$ amplitude (and the PC index) remained below a level of 2 mV/m, then there was no clear indication of directly related substorm onsets. For $E_M$ rising to amplitudes between 2 and 6 mV/m there would be a substorm onset following a growth phase where the PC and AE indices would gradually increase. The average growth phase duration varied systematically with the $E_M$ amplitude from 60 min down to 0. For $E_M$ amplitudes (and related PC levels) above 6 mV/m the substorm activity would immediately follow the $E_M$ increase without any significant delay.

A relevant question is now whether the general activity level of auroral processes as such may influence the polar cap activity level above the direct effects of the solar wind parameters, notably the merging electric field, $E_M$. Figure 16 presents the relations between

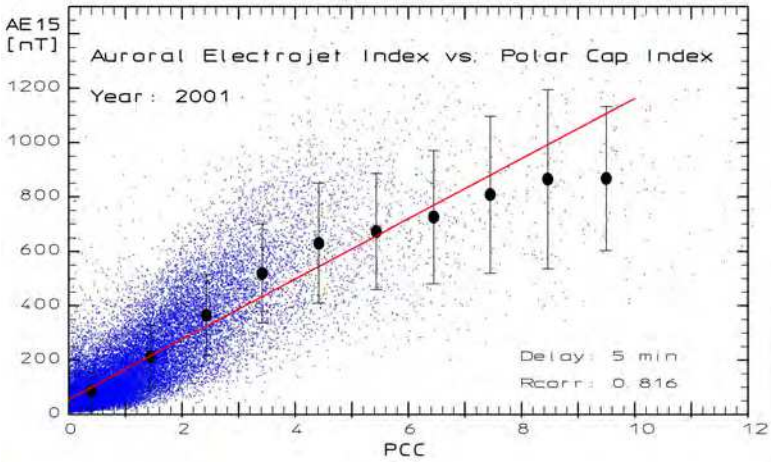


Fig. 15. Scatter plot between values of auroral electrojet indices, AE, and polar cap indices, PCC, through 2001.

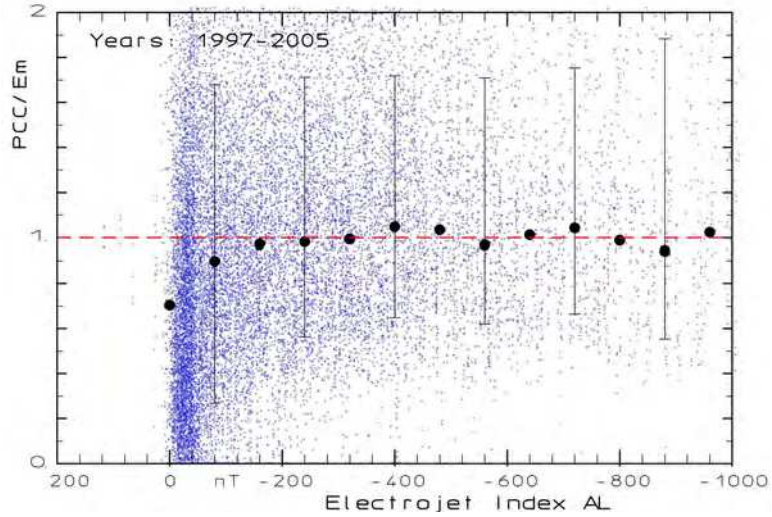


Fig. 16. Scatter plot of the ratio PCC/$E_M$ versus auroral electrojet activity index AL

the ratio of PCC over $E_M$ and the level of the (usually negative) auroral electrojet index, AL. The horizontal dashed line represents the ideal unity ratio between PCC and $E_M$. A noticeable feature is the variation from a relatively low value of PCC/$E_M$ at around 0.7 for AL values close to zero to almost unity for AL equal to -150 nT. This range comprises quiet and weakly disturbed conditions. For magnetically disturbed conditions with still larger negative values of AL beyond -150 nT, there is hardly any variation in the average ratio of PCC over $E_M$ . There is a substantial scatter in the distribution of values but the average ratio stays close to unity through the range from -150 up to -1000 nT in the auroral electrojet index, AL. Beyond that range the statistics is too sparse for conclusions. The variations in the

ratio PCC/$E_M$ at weak to moderate auroral activities (AL>-150 nT), no doubt, relate to the increase in conductivities through ionization by substorm-associated particle precipitation to reach a level adequate to support the ionospheric currents responsible for the PC indices.

A different question is whether the individual steps of the substorm cycle, comprising growth phase, onset, expansion phase, and recovery, affect the polar cap activity variations around the mean level predominantly defined by the solar wind electric field, $E_M$. In order to investigate this question we have "synchronized" PC index variations to the onset of substorms. The results are displayed in Fig. 17. The data refer to cases with steady solar wind conditions from at least 1 hour before the onset time until 2 hours after. Epoch time zero in the fields is the substorm onset time as defined by a sudden negative excursion in the AL index.

The top field displays the solar wind electric field, $E_M$, (referred to 12 Re reference position) through an interval spanning from 1 hour before to 3 hours after onset. On top of the individual traces the heavy line marks the average value. The next lower field displays the values of the auroral electrojet indices AU (upper traces) and AL (lower traces). The heavy lines mark the average values within each of the two index data sets. The sharp downward change in AL at epoch time zero is readily identified. The negative peak value in AL is reached at around 10-15 min after onset. The AU indices, notably their average values, hardly indicate any change at all. The next lower field displays the PCC index variation on the same time scale as the AU/AL display. A remarkable feature here is the peak at around 30-40 min after substorm onset, that is, at around 20-25 min after the negative peak in AL (or the corresponding positive peak in AE=AU-AL).

The bottom field repeats the average $E_M$ variations (red line) and average PCC variations (blue line) while the heavy line displays their ratio, PCC/$E_M$, using the scale to the right. It should be noted that the PCC/$E_M$ ratio has a marked minimum value of approximately 0.7 at around epoch time -30 to -20 min and a maximum value of around 1.3 at epoch time 35-40 min after onset. At 120 min there is another minimum at a value close to 0.8. Thereafter the PCC/ $E_M$ ratio approaches unity.

Using substorm terminology for the PCC/$E_M$ variations, there is clearly a "pre-onset" or "build-up" phase with minimum PCC/$E_M$ ratio prior to substorm onset. There is no steep onset but a gradual "expansion" phase with increasing ratio leading up to a peak value at 35-40 min after substorm onset. Then follows a "recovery" phase with gradual decrease in the PCC/$E_M$ ratio. In the recovery phase the ratio might have reached the low pre-onset level (0.7) at around 120 min after onset had there not been some new events at this time to raise the average PCC/$E_M$ level. These new events are spotted in the PCC plots (second field from bottom). Correspondingly, the pre-onset level is probably influenced to some degree by the increased level experienced during the recovery phase following the preceding event.

In summary of the above analyses the PC index provides a fair indicator of subsequent substorm activity. For quiet conditions with PC<~2 units there are hardly any substorm onsets. The auroral electrojet activity indices AE and AL track possible variations in the PC index. If the PC index increases from quiet to more disturbed conditions then substorm onsets are likely to occur as the PC index increases beyond ~2 units with a delay depending on the actual magnitude of the PC index, typically a few tens of minutes. If the PC index takes values above ~5 units then substorm activity follows immediately. There is some

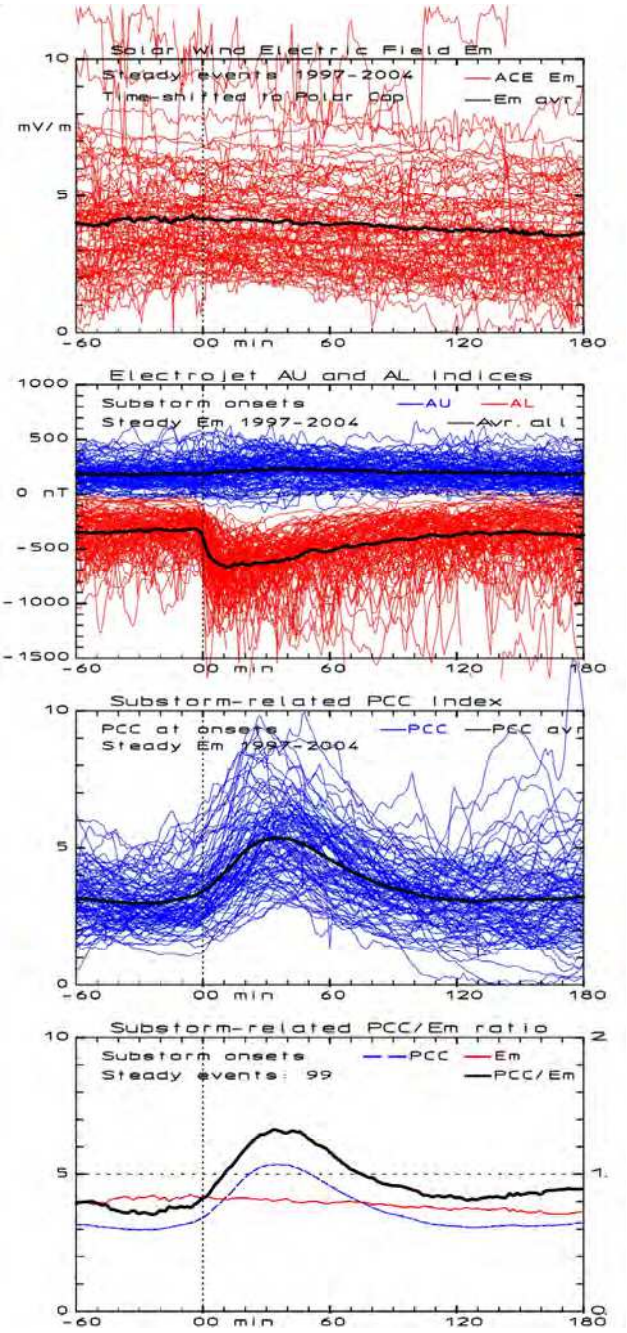


Fig. 17. Solar wind electric fields (top), AL and AU indices, PCC indices, and averages of Em and PCC and their ratio PCC/Em (bottom) for cases with steady interplanetary conditions.

coupling from auroral activity to the amplitude of the polar cap indices during weakly disturbed conditions probably related to the changes in ionospheric conductivities resulting from precipitation of substorm-associated auroral particles. The overall correlation between auroral activity represented by the AE indices and the polar cap indices, PCN or PCS, ranges between 0.60 and 0.85 depending on seasonal and solar cycle conditions. Using the combined PCC index enhances the correlation to reach an average of around 0.82.

### 6.3 Relations between PC indices and Joule and auroral particle heating

The thermosphere, particularly in the auroral regions, is heated by the amount of energy deposited by Joule heating and by precipitating particles. The heating generates thermospheric vertical motions and composition changes. The associated expansion of the atmosphere could have grave consequences for the tracking of satellites and for other spacecraft operations through the varying drag on space objects.

In various models to calculate drag coefficients, parameters such as the F10.7 cm flux (proxy for solar EUV radiation), the planetary Kp index, or the auroral electrojet index have been used to derive Joule heating values (e.g., Tobiska et al., 2008). Further attempts to calculate Joule heating include estimates of Joule heating in response to IMF input based on large-scale modelling of electrodynamic parameters (e.g., Chun et al., 1999, 2002; Weimer, 2005; Weimer et al., 2011).

Attempts to relate Joule heating to the polar cap index were reported by Chun et al. (1999, 2002). Basically they have derived hemispheric Joule heat production rates from the "Assimilative Mapping of Ionospheric Electrodynamics" (AMIE) procedure through a number of well documented storms. The AMIE procedure uses data from a large number of magnetometers, coherent and incoherent radars, digisondes and satellites with instruments for detection of electron precipitation and electric fields, to produce global patterns of various electrodynamic parameters. AMIE calculates Joule heating rate (jh) as shown in Eq. 17:

$$jh = \Sigma_P E^2 \tag{17}$$

where $\Sigma_P$ is the ionospheric height-integrated Pedersen conductivity and E the electric field. The Joule heating may be integrated over either hemisphere or globally to produce the total Joule heating power. From the study by Chun et al. (1999), the total Joule heating power for the northern hemisphere (JH) was estimated for each season separately and compared to the corresponding values of the polar cap index, PCN. Their results are shown in Eqs. 18a-d:

$$\text{Winter:} \quad JH = 4.84\ PCN^2 + 16.9\ PCN + 5.6 \quad [GW] \tag{18a}$$

$$\text{Equinox:} \quad JH = 4.14\ PCN^2 + 25\ PCN + 8.9 \quad [GW] \tag{18b}$$

$$\text{Summer:} \quad JH = 14.39\ PCN^2 + 23.7\ PCN + 11.5 \quad [GW] \tag{18c}$$

$$\text{All data:} \quad JH = 4.03\ PCN^2 + 27.3\ PCN + 7.7 \quad [GW] \tag{18d}$$

Chun et al. (1999) noted that the expressions are valid also for negative values of the PCN index, which may occur during reverse convection cases, particularly during the summer season. Further, they compared the results of the above modelling (Eqs. 18a-d) with the

simpler models based on either the cross polar cap voltage, $\Phi_{PC}$, or the Auroral electrojet indices, AE, and found them about equally representative for the AMIE-derived Joule heating rates. This result is not so surprising since the cross polar cap potentials as well as the auroral electrojet indices are closely correlated with the polar cap indices as demonstrated in the previous sections.

From Thule PCN data and NOAA SPW Hemispheric Auroral Power (AP) data based on measurements from NOAA POES satellites through the years 1999-2002, and selecting only the northern passes, we have prepared the scatter plot displayed in Fig. 18. The heavy dots mark averages of AP values (in GW) through every unit of the PCN index. From Fig. 21 one may note the minimum in average AP around 10 GW at PCN = 0. The AP values are increasing both for increasing negative and positive PCN values but there is a marked difference between the slopes for positive and negative index values. The slopes for negative index values, particularly for the summer data, are much lower than those for the positive index data. For positive index values the average variations could be described by Eqs. 19a-c:

$$\text{Winter:} \quad AP = 13.5\ PCN + 10 \quad [GW] \tag{19a}$$

$$\text{Equinox:} \quad AP = 13.5\ PCN + 10 \quad [GW] \tag{19b}$$

$$\text{Summer:} \quad AP = 11.5\ PCN + 10 \quad [GW] \tag{19c}$$

These results are not so different from those reported by Chun et al. (2002) taking into account that they did not discriminate against negative PCN index values, which they – looking at their data (their Fig. 9) - might well have done.

Summarizing from the above analyses, there appears to be quite consistent relations between the PC indices and the heating of the thermosphere by Joule heating as well as by

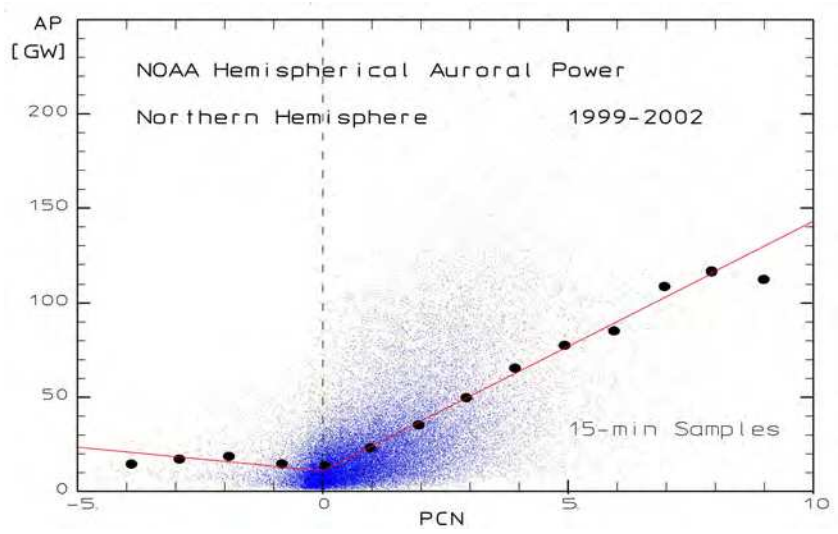


Fig. 18. Scatter plot of Northern Hemispheric Auroral Power data vs. PCN index values.

auroral particle precipitation. There are marked differences between cases with positive (forward convection) and negative (reverse convection) PC index values. Such differences are probably caused by the much reduced size of the active auroral and polar cap regions for the northward IMF Bz cases that causes the major part of the negative PCN values.

### 6.4 Relations between PC indices and the ring current

The Earth is encircled by currents flowing near equator at distances of typically 4-6 Re. These currents could be divided into the symmetrical part (RCS) that is formed all the way around the Earth, mostly by drifting mirroring energetic electrons and ions, and the partial ring current (RCP). Referring to Fig. 1, field-aligned Region 1 (R1) currents flow from the dawn magnetospheric boundary regions to the ionosphere at the morning side. Part of this current flows equatorward across the auroral region to feed the upward Region 2 (R2) field aligned currents (FACs) emerging from lower latitudes. The R2 FACs flow to the ring current region and add to the ring current at the night side to form a partial ring current. From the evening side of the ring current region, the R2 FACs flow to the ionosphere; part of these currents flows poleward crossing the auroral region and add to the R1 FACs leaving the ionosphere to end at the dusk boundary regions. It is also possible that a substantial part of the partial ring current is built from electrons and ions that simply drift directly between the magnetospheric dawn and dusk boundary regions across the near-tail region.

The ring current intensities are detected from a network of low-latitude magnetometer stations whose data are sent to World Data Centre WDC-C2 in Kyoto and processed to provide indices for the symmetrical as well as the partial ring currents (Sugiura & Kamei, 1981). The hourly symmetrical deflections scaled from the horizontal (H) components give the Dst index. The corresponding symmetrical index scaled from 1-min values of the H components provides the SYM-H index while the corresponding scaling of 1-min values of the D components generates the SYM-D index. Similarly the asymmetrical parts of the 1-min H and D components generate the ASY-H and ASY-D indices.

The asymmetric ring current index, ASY-H, have been provided by WDC-C2 (Iyemori et al., 2000) as 1-min values. For the present statistical study a less detailed time resolution, which reduces the inherent scatter in the data, is considered appropriate. Hence, the ASY-H and the polar cap indices, PCC, have been averaged to form 5-min samples. The two parameter sets have been subjected to linear correlation analysis using a stepwise variable delay between samples of the respective time series assuming that the most appropriate delay gives maximum value of the correlation coefficient. With this delay imposed on all pairs of samples of the time series, a linear relation between two parameter sets is found by least squares regression analysis. The average deviation, S0, the numerical deviation, S1, and the RMS standard deviation, S2, are calculated from the assumed linear relation.

Figure 19 displays ASY-H against PCC. The 15 min delay noted in the figure was found to provide optimum correlation (Rx=0.743). The regression line plotted in the diagram characterizes ASY-H against PCC. For this relation, the scatter parameters, S0, S1, and S2, are listed in the figure. The standard deviation (S2) is ~18 nT. A noteworthy feature in the display is the persistent linear relations of the average ASY-H values on PCC (Eq. 20) up to high levels

$$\text{ASY-H} = 12.1\ \text{PCC} + 11.5\ [\text{nT}] \tag{20}$$

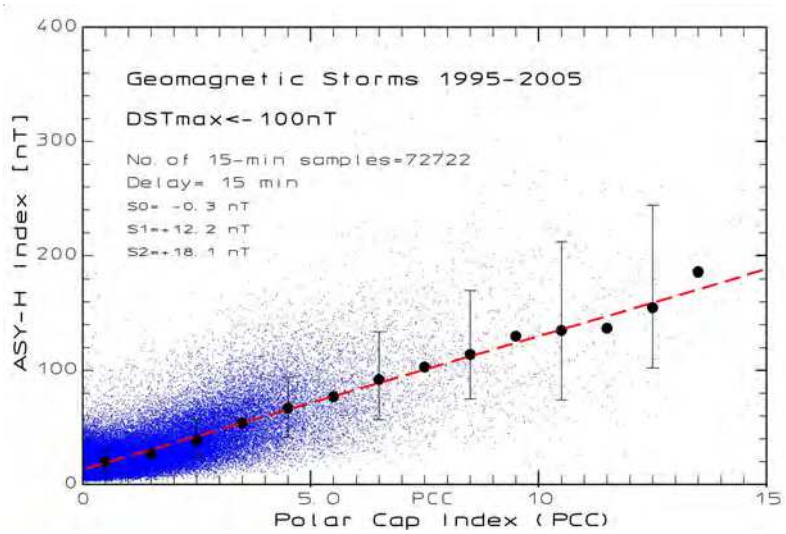


Fig. 19. Scatter plot of ASY-H partial ring current index vs. polar cap PCC index.

The Dst ring current index is closely related to the presence of energetic electrons and ions, notably $H^+$ and $O^+$, in the inner magnetosphere. Their different drift motion, positive ions westward and electrons eastward, in the geomagnetic dipole-like field contributes a net westward electric current. A succesful relation between the accumulated kinetic energy of the charged particles and the Dst* index is provided by the Dessler-Parker-Sckopke relation (Dessler & Parker, 1959; Sckopke, 1966) in Eq. 21:

$$\text{Dst}^*[\text{nT}] = 4.0 \cdot 10^{-30} E_{RC}\,[\text{keV}] \tag{21}$$

where Dst* is the Dst index corrected for the contributions from magnetopause currents (MPC) while $E_{RC}$ is the total kinetic energy of particles trapped in the ring current region.

Thus, the Dst index represents the energy stored in the ring current. Hence the merging electric field, $E_M$, or, equivalently, the polar cap PC index should be considered to represent a source function for the Dst index rather than being related to its current value. Following Burton et al. (1975) the change in the Dst index with time could be written:

$$d\text{Dst}^*/dt = Q - \text{Dst}^*/\tau\ [\text{nT/hr}] \tag{22}$$

where Q in Eq. 22 is the source term while the last term is the ring current loss function controlled by the decay time constant $\tau$ here measured in hours. For the small actual MPC corrections, the Dst dependent statistical values provided in Joergensen et al. (2004) are used while the decay function given in Feldstein et al., (1984) is used for the loss term. This function uses two decay time constants, $\tau$ = 5.8 hrs for large disturbances where Dst < -55 nT, and $\tau$ = 8.2 hrs for small disturbances where Dst > -55 nT. Now, the relation in Eq. 22 has only terms relating to the source function Q and to the observed initial Dst index values.

In Burton et al. (1975) the source term Q is related to the $Y_{GSM}$ component of the solar wind electric field. In the analysis by Stauning (2007), in addition to the dependence on $E_M$, the

relation of Q to the polar cap index PCC was examined for a number of storm event cases during the interval 1995-2002. Here we repeat these analyses using selected large storm events through 1995-2005. In all these cases we first derive the temporal change at time t=T in the hourly Dst* index from the hourly values at t=T-1 and t=T+1 [hrs] by the simple differential term:

$$dDst^*/dt\ (T) = (Dst^*(T+1) - Dst^*(T-1))/2.\ [nT/hr] \quad (23)$$

In order to derive the source function, Q, to be used in Eq. 22, the average slope values defined by Eq. 23 are corrected by adding the decay term defined above using the current Dst* value at t=T. The resulting source function, $Q_{obs}$, is then related to the potential source parameters with a variable positive or negative delay imposed on the relation. The parameters, the PC indices, are provided at a more detailed time resolution (typically 1-min) than the hourly source function values. By shifting the averaging interval by delays varying on minute scale, hourly averages of the parameters are correlated with the hourly source function values to derive the delay that produces the maximum correlation through the ensemble of storm events. With this delay the best fit linear relation between the source function values and the relevant source parameter is determined by linear regression analysis.

The scatter plots in Fig. 20 present the Dst* source function, $Q_{obs}$ , based on observed hourly Dst values plotted against the combined polar cap index, PCC, as a potential source parameter. The relation between the best fit "equivalent" source function, $Q_{eq}$, and the source parameter values, PCC, is then expressed in a linear function:

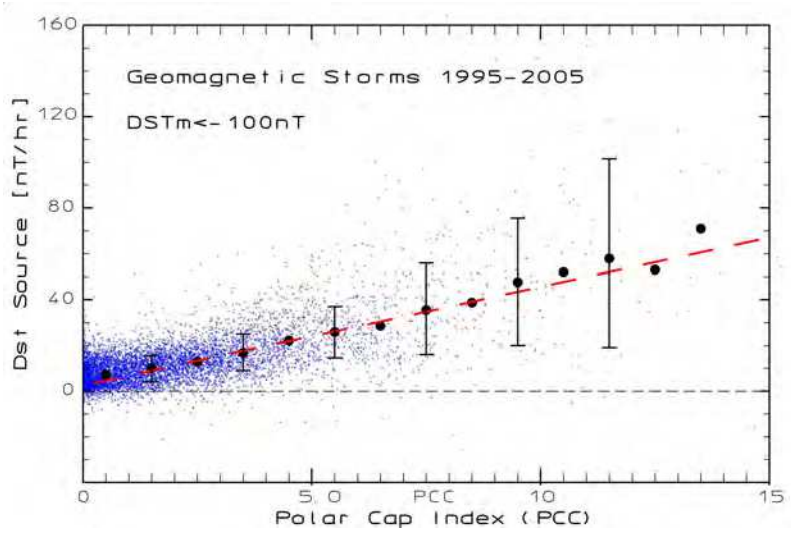


Fig. 20. Scatter plot of Dst* source function vs. polar cap PCC index.

$$Q_{eq} = 4.6\ PCC + 1.2\ [nT/h] \quad (24)$$

with standard deviation equal to 9.4 nT/h.

With continuous time series of source parameter values, specification of the relational constants appearing in Eq. 24, and initial Dst values, it is now possible to integrate Eq. 22 to derive values of an "equivalent" Dst index, $Dst_{eq}$, through any interval of time. The procedure has been applied to the major geomagnetic storms (Dst<-100 nT) occurring through cycle 23. For each storm interval the calculations have been carried through intervals of 4 days. For each interval the equivalent Dst series was given an initial value equal to the observed Dst at the start of the first day, while all later $Dst_{eq}$ values through the 4 days were derived solely from the integration of Eq. 22 without attachment to observed Dst values.

Figure 21 displays an example for the case of a moderate geomagnetic storm on 7 – 10 April 1995. The peak (negative) Dst value is -150 nT observed at 1800 UT on 7.4.1995. In the figure the observed Dst values are displayed in black line with "dots" and located in the lower part of the diagram. The merging electric field, $E_M$, is displayed in thin green line in the upper half of the diagram. By its definition $E_M$ is non-negative. Values of the PCC index (also non-negative) are displayed in thin blue line with small squares while values of the asymmetric ring current index, ASY-H, are displayed in red line with crosses mainly in the upper part. Values of the equivalent Dst index calculated from the PCC indices are shown in blue line with squares.

The merging electric field, Em, and the asymmetric index, ASY-H have also been used as source functions similarly to the above derivation of the Dst indices using the PCC indices. Values of the equivalent Dst index calculated from $E_m$ are displayed in the thin green line in

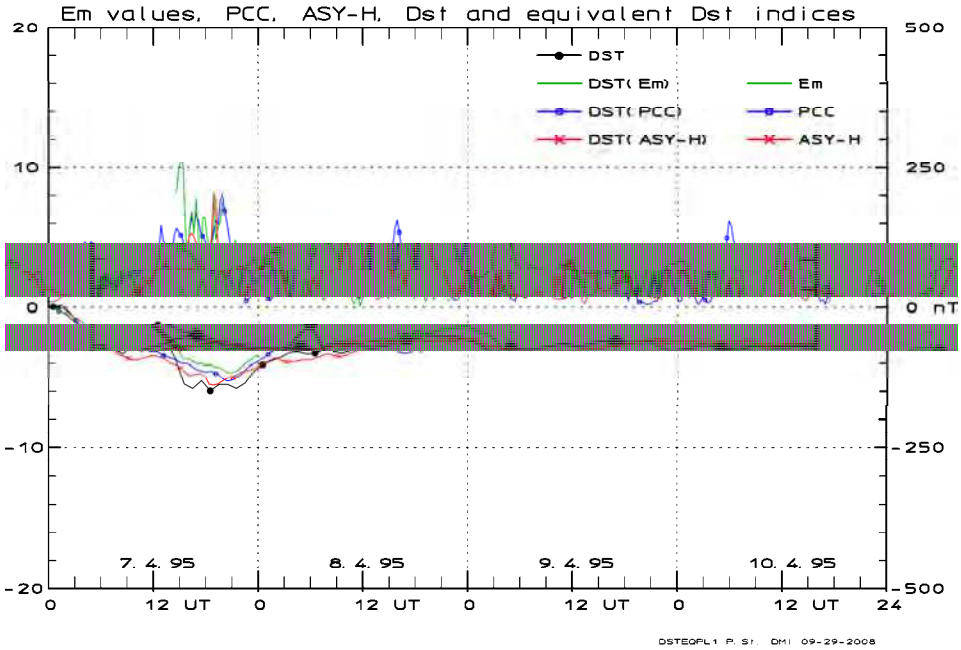


Fig. 21. Display of parameters $E_M$, PCC, ASY-H (in upper half of fields), and observed ring current index, Dst, and derived ring current indices $Dst_{eq}(E_M)$, $Dst_{eq}$ (PCC), and $Dst_{eq}$ (ASY-H)

the lower part. In this case the series of equivalent Dst values based on $E_m$ terminates after the first day since there is a break in the $E_M$ data at midnight between 7 and 8 April 1995. The equivalent Dst indices using ASY-H in the source function are displayed in red line with crosses through all 4 days. In this case the PCC and the ASY-H index data are continuously available for the integration of Eq. 22 throughout the storm interval.

It is clear from Fig. 21 that there is good agreement between the observed and the equivalent Dst values throughout the 4 days of integration. A similar case is displayed in Fig. 22. The PCS index was not available for the storm. Hence, here the calculations were based solely on the PCN index series. Based on the peak values of the Dst index, this case illustrates one of the strongest geomagnetic storm events of cycle 23. Generally, going from the moderate to the strong storm cases gives less agreement between observed and equivalent Dst values. There is no clear indication in these plots whether the equivalent Dst values based on $E_M$ are better or worse than those based on PCC, PCN, AL or ASY-H.

In order to resolve the question whether using $E_M$, PCC, PCN, AL or ASY-H in the source function give better agreement the average differences and variances between the observed and the equivalent Dst values were calculated for all cases studied. The results are listed in Table 3. It should be noted that the data sets forming the basis for $Dst_{eq}$ calculations are not completely identical since the $E_M$ data are often interrupted temporarily or non-existing for the storm cases. The reason for the lack of $E_M$ data is often the disabling of the solar wind

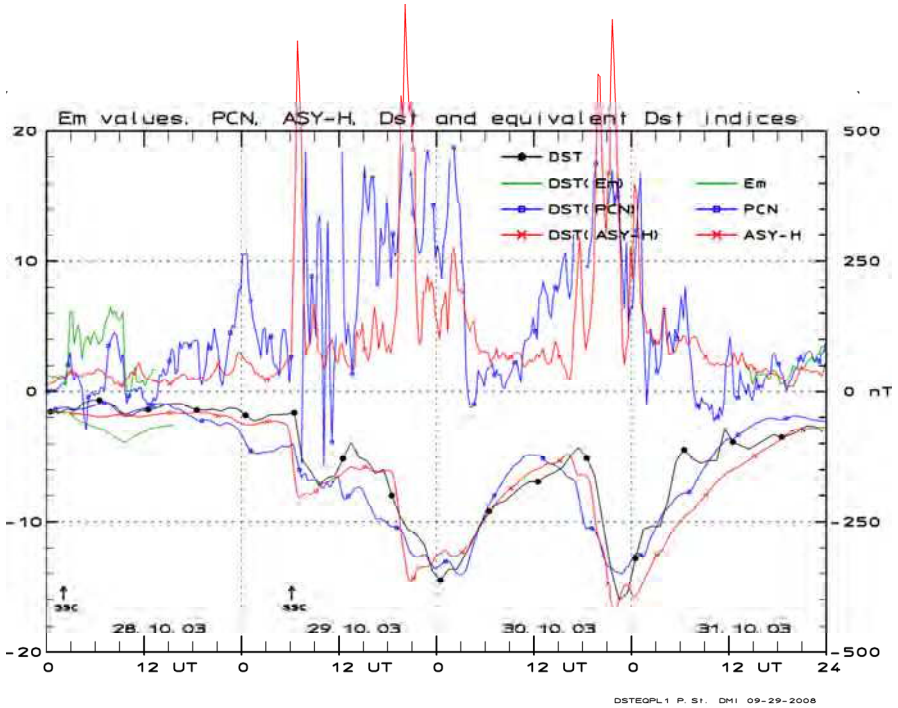


Fig. 22. Observed Dst and equivalent Dst values calculated from PCN, $E_M$ and ASY-H, respectively, through a major magnetic storm of cycle 23.

detectors by strong high-energy solar proton fluxes. Hence the equivalent Dst values based on $E_M$ data are often available during the first part of the storm interval only and the total number of samples is considerably reduced (cf. Table 3). Since the integration extending through 4 days becomes less and less certain with increasing interval length this preference for the first days may give the $E_M$-based $Dst_{eq}$ values an advantage in the correlation with Dst over the PCC, PCN, AL or ASY-H-based values.

| Parameter\Source | $E_M$ field | PCC index | PCN index | AL index | ASY-H index |
|---|---|---|---|---|---|
| No. samples | 3992 | 7776 | 8640 | 7968 | 8640 |
| Avr. deviation | -7.6 | 1.8 | 2.7 | 11.5 | - 4.9 nT |
| Std. deviation | 27.6 | 30.6 | 31.4 | 34.2 | 24.7 nT |

Table 3. Equivalent Dst versus observed Dst index through major geomagnetic storms 1995-2005

The best source function when comparing the average deviation between the observed Dst and the calculated equivalent values is provided by the PCC index series. Best to reduce the variance (standard deviation) is the ASY-H index followed by the solar wind merging electric field, $E_M$. The PCC index series gives larger variance than $E_M$ but is continuously available in twice the number of cases. PCN based on Thule data are virtually available continuously. Thus, the PC indices, particularly the PCC index series, may serve to calculate the ring current indices, Dst, SYM-H, and ASY-H, in real time if the magnetic data from Thule and eventually Vostok are available on-line.

## 7. Conclusions

The polar caps provide terrestrial "windows" to the solar wind and enable monitoring of the merging electric field, $E_M$, the most important parameter for transfer of energy and momentum from the solar wind into the Earth's environment. The intruding solar wind energy is used to power a range of geophysical processes such as the large-scale electric potential patterns and the associated convection and current systems in the high-latitude magnetospheric and ionospheric regimes. The intensities of the transpolar ionospheric currents are very well suited to monitor the solar wind electric field. The associated magnetic disturbances at ground, when properly scaled to compensate for the regular daily and seasonal variations in conductivities, provide the polar cap index, PC, which can serve as a proxy for the merging electric field.

In addition, the PC indices, in particular when available from both polar caps, may serve to indicate the level of further geophysical disturbances such as polar ionospheric electric fields and plasma motions, auroral activities characterized, for instance, by the auroral electrojet indices (AL, AU, and AE), heating of the upper atmosphere by Joule dissipation (JH) and particle precipitation (AP), mid-latitude magnetic disturbances characterized by the Kp index, and the development of partial and symmetrical ring currents in the equatorial regions characterized by the Dst, the SYM-H, and the ASY-H indices. Such disturbances constitute an essential part of the conditions termed "Space Weather".

The polar cap indices are derived from a single station in each hemisphere, Thule in the northern polar cap and Vostok in the southern, both of which provide the basic magnetic data

in high resolution and on-line in real time. These characteristics could be contrasted to those applicable to other indices used to characterize geophysical disturbances such as the auroral electrojet indices requiring data from 8-12 observatories to provide a reliable index, or the ring current indices based on 4-6 observatories. The estimation of Joule or particle heating power need either an extended network of magnetometer stations to run the AMIE procedure or polar satellite passes to derive the transpolar potential structure and the intensities of precipitating particles. Even in comparison with observations from interplanetary satellites, the monitoring of disturbances through the polar cap indices provides the advantage of not being affected by the intense high-energy particle radiation that often accompany the strong solar outburst, where the reliable monitoring of possible geophysical disturbances, that is, adverse space weather conditions, is particularly important.

## 8. Acknowledgments

The author is indebted to the observatory staffs for their dedicated efforts to provide magnetic data of utmost quality and continuity from the DMI geomagnetic observatory in Qaanaaq (Thule), Greenland, and the AARI geomagnetic observatory in Vostok at Antarctica. The author gratefully acknowledges the access to IMP8, Geotail, WIND and ACE satellite data on solar wind plasma and magnetic field observations provided through the NSSDC and the Caltech Research Laboratory data centres. We are also indepted to the NOAA SWP for supplying the NOAA POES satellite data. Furthermore, we gratefully acknowledge the access to Dst, SYM, ASY, and Auroral Electrojet indices from WDC-C2 at Kyoto University and express our deep appreciation of the efforts invested in the collection and processing of the geomagnetic data.

## 9. References

Akasofu, S.-I. (1979). Interplanetary energy flux associated with magnetospheric substorms, doi:10.1016/0032-633(79)90119-3, *Planet. Space Sci.*, 27, 425.

Araki, T. (1994). A physical model of geomagnetic sudden commencement, in: *Solar Wind sources of Magnetospheric Ultra-Low-Frequency Waves*, Geophys. Monogr. 81, eds.: M.J. Engebretson et al., pp. 183-200, AGU, Washington, D.C.

Borovsky, J. E., Layraud, B. & Kuznetsova, M. M. (2009). Polar cap potential saturation, dayside reconnection, and changes to the magnetosphere, *J. Geophys. Res.,* 114, A03224, doi:10.1029/2009JA014058.

Boyle, C. B., Reiff, P. H. & Hairston, M. R. (1997). Empirical polar cap potentials, *J. Geophys. Res.*, 102, 111.

Burton, R. K., McPherron, R. L., & Russell C. T. (1975). An empirical relationship between interplanetary conditions and Dst, *J. Geophys. Res.*, *80*, 4204-4214.

Chun, F. K., Knipp,D. J., McHarg, M. G., Lu, G., Emery, B. A., Vennerstrøm, S. & Troshichev, O. A. (1999). Polar cap index as a proxy for hemispheric Joule heating, *Geophys. Res. Lett.*, 26 , 1101-1104.

Chun, F.K., Knipp, D. J., McHarg, M. G., Lacey, J. R., Lu, G., & Emery, B. A. (2002). Joule heating patterns as a function of polar cap index, *J. Geophys. Res.*, *107* (A7), doi:10.1029/2001JA000246.

Davis, T. N. & Sugiura, M. (1966). Auroral electrojet activity index AE and its Universal Time variations, *J. Geophys. Res*. 71, 785.

Dessler, A. J. & Parker, E. N. (1959). Hydromagnetic theory of geomagnetic storms, *J. Geophys. Res.*, *64*, 2239-2259.

Fairfield, D. H. (1968). Polar magnetic disturbances and the interplanetary magnetic field, *COSPAR Space Research VIII*, 107.

Farris, M.H. & Russell, C. T. (1994). Determining the standoff distance of the bow shock: Mach number dependence and use of models, *J. Geophys. Res*., 99, 17681-17689.

Feldstein, Y. I., Pisarsky, V. Yu, Rudneva, N. M. & Grafe, A. (1984). Ring current simulation in connection with interplanetary space conditions, *Planet. Space Sci*, *32*, 975-984.

Fiori, R. A. D., Koustov, A. V., Boteler, D. & Makarevich, R. A. (2009). PCN magnetic index and average convection velocity in the polar cap inferred from SuperDARN radar measurements, *J. Geophys. Res*. 114, A07225, doi:10.1029/2008JA013964.

Friis-Christensen, E. & Wilhjelm, J. (1975). Polar cap currents for different directions of the interplanetary magnetic field in the Y-Z plane, *J. Geophys. Res*., 80, 1248-1260.

Fukushima, N. (1976). Generalized theorem for no ground magnetic effect of vertical currents connected with Pedersen currents in the uniform-conductivity ionosphere, *Rep. Ionos. Space Res. Jpn*., 30, 35.

Greenwald, R. A., Bristow, W. A., Sofko, G. J., Senior, C., Ceriser, J.-C. & Szabo, A. (1995). SuperDual Auroral Radar Network radar imaging of dayside high-latitude convection under northward interplanetary magnetic field: Toward resolving the distorted two-cell versus multicell controversy, *J. Geophys. Res*., 100, 19.661.

Hairston, M. R., Heelis, R. A., & Rich, F. J. (1998), Analysis of the ionospheric cross polar cap potential drop using DMSP data during the National Space Weather Program study period, *J. Geophys. Res*., 103, 26,337.

Hairston, M. R., Drake, K. A., and Skoug, R. (2005). Saturation of the ionospheric polar cap potential during the October-November 2003 superstorms, *J. Geophys. Res*., 110, A09826, doi:10.1029/2004JA010864.

Huang, C.-S. (2005). Variations of polar cap index in response to solar wind changes and magnetospheric substorms, *J. Geophys. Res*., 110, A01203, doi:10.1029/2004JA10616.

Iijima, T. & Potemra, T. A. (1976a). The amplitude distribution of field-aligned currents at northern high latitudes observed by Triad, *J. Geophys. Res*., 81, 2165-2174.

Iijima, T. & Potemra, T. A. (1976b). Field-aligned currents in the dayside cusp observed by Triad, *J. Geophys. Res*., 81, 5971.

Iyemori, T., Araki, T., Kamei, T. & Takeda, M. (2000). Mid-latitude geomagnetic indices "ASY" and "SYM" for 1999, *Geomagnetic indices home page*, ed.: T. Iyemori, (http://swdcwww.kugi.kyoto-u.ac.jp/dstdir/index.html), WDC-C2 for Geomagnetism, Kyoto University.

Janzhura, A, Troshichev, O. A. & Stauning, P. (2007). Unified PC indices: Relation to isolated magnetic substorms, *J. Geophys. Res*., 112, A09207, doi:10.1029/2006JA012132.

Jorgensen, A. M., Spence, H. E., Hughes, W. J. & Singer, H. J. (2004). A statistical study of the ring current, *J. Geophys. Res*., *109*, A12204, doi:10.1029/2003JA010090.

Kan, J. R. & Lee, L. C. (1979). Energy coupling function and solar wind-magnetosphere dynamo, *Geophys. Res. Lett*., *6*, 577.

Kuznetsov, B. M. and Troshichev, O. A. (1977). On the nature of polar cap magnetic activity during undisturbed periods, *Planet. Space Sci*., 25, 15–21, 1977.

Lukianova, R., Troshichev, O. A. & Lu, G. (2002). The polar cap magnetic activity indices in the southern (PCS) and northern (PCN) polar caps: Consistency and disrepancy, Geophys. Res. Lett., 29(18), 1879, doi:10.1029/2002GL015179.

Lukianova, R. (2003). Magnetospheric response to sudden changes in the solar wind dynamic pressure inferred from polar cap index, *J. Geophys. Res.*, *108* (A12), 1428, SMP-11. doi:10.1029/2002JA009790.

Mansurov, S. M. (1969). A new evidence of connection between Space and Earth's magnetic fields, *Geomag. and Aeron*., 9, 768.

Newell, P. T. & Meng, C.-I. (1994). Ionospheric projections of magnetospheric regions under low and high solar wind pressure conditions, *J. Geophys. Res.*, *99* (A1), 273-286.

Reiff, P. H., Spiro, R. W. & Hill, T. W. (1981). Dependence of polar cap potential drop on interplanetary parameters, *J. Geophys. Res.*, 86, 7639.

Rich, F. J., & Hairston, M. (1994). Large-scale convection patters observed by DMSP, *J. Geophys. Res.*, 99, 3827.

Sckopke, N. (1966). A general relation between the energy of trapped particles and the disturbance field near the Earth, *J. Geophys. Res.*, *71*, 3125-3130.

Shue, J.-H., Chao, J. K., Fu, H. C., Russell, C. T., Song, P., Khurana, K. K. & Singer, H. J. (1997). A new functional form to study the solar wind control of the magnetopause size and shape, *J. Geophys. Res*., 102, 9497-9511.

Siscoe, G. L., Crooker, N. U. & Siebert, K. D. (2002). Transpolar potential saturation: Roles of region 1 current system and solar wind ram pressure, *J. Geophys. Res*. 107 (A10), 1321, doi:10.1029/2001JA009176.

Sonnerup, B. (1974). Magnetopause reconnection rate, *J. Geophys. Res*., 79, 1546-1549.

Spreiter, J. R., Summers, A. L. & Alksne, A. Y. (1966). Hydromagnetic flow around the magnetosphere, *Planet. Space Sci*., *14*, 223-253.

Stauning, P., Troshichev, O. A. & Janzhura, A. (2006). Polar Cap (PC) index. Unified PC-N (North) index procedures and quality. *DMI Scientific Report, SR-06-04.* (available at www.dmi.dk/publications/sr06-04.pdf).

Stauning, P., (2007). A new index for the interplanetary merging electric field and geomagnetic activity: Application of the unified polar cap indices, *Space Weather*, *5*, S09001, doi:10.1029/2007SW000311.

Stauning, P. & Troshichev, O. A. (2008). Polar cap convection and PC index during sudden changes in solar wind dynamic pressure, *J. Geophys. Res*., 113, doi:10.1029/2007JA012783.

Stauning, P., Troshichev, O. A. & Janzhura, A. (2008). The Polar Cap (PC) index:. Relations to solar wind parameters and global activity level, *J. Atmos. Solar-Terr. Phys*., doi:10.1016/j.jastp.2008.09.028.

Stauning, P. (2011), Determination of the quiet daily geomagnetic variations for polar regions, *J. Atmos. Solar-Terr. Phys*., doi:10.1016/j.jastp.2011.07.004.

Sugiura, M. & Davis, T. N. (1966). Auroral electrojet activity index AE and its universal time variations, *J. Geophys. Res., 71*, 785-801.

Sugiura, M. & Kamei, T. (1981). Description of the hourly Dst index, in: *Geomagnetic indices home page*, ed.: T. Iyemori, (http://swdcwww.kugi.kyoto-u.ac.jp/dstdir/index.html), WDC-C2 for Geomagnetism, Kyoto University.

Svalgaard, L. (1968). Sector structure of the interplanetary magnetic field and daily variation of the geomagnetic field at high-latitudes, *Scientific Report, R-8*, Danish Meteorological Institute.

Svalgaard, L., (1972). Interplanetary magnetic sector structure 1926-1971, *J. Geophys. Res*., 77, 4027.

Svalgaard, L., (1973). Polar cap magnetic variations and their relationship with the interplanetary magnetic sector structure, *J. Geophys. Res*., 78, 2064-2078.

Tobiska, W. K., Bouwer, S. D. & Bowman, B. R. (2008). The development of new solar indices for use in thermospheric density modelling, *J. Atmos. Solar-Terr. Phys*., 70, 803-819.

Troshichev, O. A., Dmitrieva, N. P. & Kuznetsov, B. M. (1979). Polar Cap magnetic activity as a signature of substorm development, *Planet. Space Sci*., 27, 217.

Troshichev, O. A. & Andrezen, V. G. (1985). The relationship between interplanetary quantities and magnetic activity in the southern polar cap, *Planet. Space Sci*., 33, 415.

Troshichev, O. A., Kotikov, A. L., Bolotinskaya, B. D., Andrezen, V. G. (1986). Influence of IMF azimuthal component on magnetospheric substorm dynamics, *J. Geomagn. Geoelectr*., 38, 1075.

Troshichev, O. A., Andrezen, V. G., Vennerstrøm, S. & Friis-Christensen, E. (1988). Magnetic activity in the polar cap – A new index, *Planet. Space Sci., 36*, 1095.

Troshichev, O., Hayakawa, H., Matsuoka, A., Mukai, T. & Tsuruda, K. (1996). Cross polar cap diameter and voltage as a function of PC index and interplanetary quantities, *J. Geophys. Res*., *101*, 13,429.

Troshichev, A. O., Lukianova, R. Y., Papitashvili, V. O., Rich, F. J. & Rasmussen, O. (2000). Polar Cap index (PC) as a proxy for ionospheric electric field in the near-pole region, *Geophys. Res. Lett.*, 27, 3809.

Troshichev, O. A., Janzhura, A. & Stauning, P. (2006). Unified PCN and PCS indices: method of calculation, physical sense and dependence on the IMF azimuthal and northward components, *J. Geophys. Res., 111*, A05208, doi:10.1029/2005JA011402.

Troshichev, O. A., Janzhura, A. & Stauning, P. (2007). Magnetic activity in the polar caps: Relation to sudden changes in the solar wind dynamic pressure, *J. Geophys. Res.*, 112, A11202, doi10.1029/2007JA012369.

Vennerstrøm, S. (1991). The geomagnetic activity index PC, PhD Thesis, *Scientific Report 91-3*, Danish Meteorological Institute, 105 pp.

Vennerstrøm, S., Friis-Christensen, E., Troshichev, O. A. & Andrezen, V. G. (1991). Comparison between the polar cap index PC and the auroral electrojet indices AE, AL and AU, *J. Geophys. Res., 96*, 101.

Weimer, D. R. (2005). Improved ionospheric electrodynamics models and application to calculating Joule heating rates, *J. Geophys. Res*., 110, A05306, doi:10.1029/2004JA010884.

Weimer, D. R. & King, J. H. (2008). Improved calculations of interplanetary magnetic field phase front angles and propagation time delays, *J. Geophys. Res*., 113, A01105, doi:10.1029/2007JA012452.

Weimer, D. R., Clauer, C. R., Engebretson, M. J., Hansen, T. L., Gleisner, H., Mann, I. & Yumoto, K. (2010). Statistical maps of geomagnetic perturbations as a function of the interplanetary magnetic field, *J. Geophys. Res*., 115, A10320, doi:10.1029/2010JA015540.

Weimer, D. R., Bowman, B. R., Sutton, E. K. & Tobiska, W. K. (2011). Predicting global average thermospheric temperature changes resulting from auroral heating, *J. Geophys. Res*., 116, A01312, doi:10.1029/2010JA015685.

Wilhjelm, J., Friis-Christensen, E., Potemra, T. A. (1972). The relationship between ionospheric and field-aligned currents in the dayside cusp, *J. Geophys. Res*. 83, 5586.

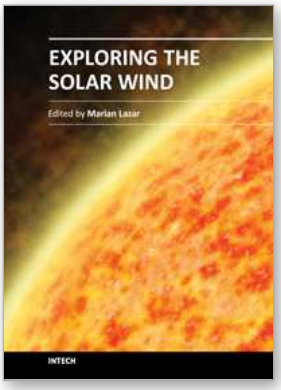


**Exploring the Solar Wind**
Edited by Dr. Marian Lazar

ISBN 978-953-51-0339-4
Hard cover, 462 pages
**Publisher** InTech
**Published online** 21, March, 2012
**Published in print edition** March, 2012

This book consists of a selection of original papers of the leading scientists in the fields of Space and Planetary Physics, Solar and Space Plasma Physics with important contributions to the theory, modeling and experimental techniques of the solar wind exploration. Its purpose is to provide the means for interested readers to become familiar with the current knowledge of the solar wind formation and elemental composition, the interplanetary dynamical evolution and acceleration of the charged plasma particles, and the guiding magnetic field that connects to the magnetospheric field lines and adjusts the effects of the solar wind on Earth. I am convinced that most of the research scientists actively working in these fields will find in this book many new and interesting ideas.



**InTech Europe**
University Campus STeP Ri
Slavka Krautzeka 83/A
51000 Rijeka, Croatia
Phone: +385 (51) 770 447
Fax: +385 (51) 686 166
www.intechopen.com

**InTech China**
Unit 405, Office Block, Hotel Equatorial Shanghai
No.65, Yan An Road (West), Shanghai, 200040, China
中国上海市延安西路65号上海国际贵都大饭店办公楼405单元
Phone: +86-21-62489820
Fax: +86-21-62489821